ATLAS CONF Note

ATLAS-CONF-2024-005

27th March 2024

Search for non-resonant Higgs boson pair production in final states with leptons, taus, and photons in pp collisions at $\sqrt{s}$ = 13 TeV with the ATLAS detector

The ATLAS Collaboration

A search is presented for non-resonant Higgs boson pair production, targeting the $bbZZ$, $4V$ ($V = W$ or Z), $VV\tau\tau$, 4τ, $\gamma\gamma VV$ and $\gamma\gamma\tau\tau$ decay channels. Events are categorised based on the multiplicity of light charged leptons (electrons or muons), hadronically decaying taus, and photons. The search is based on a dataset of proton-proton collisions at $\sqrt{s}$ = 13 TeV recorded with the ATLAS detector during Run 2 of the Large Hadron Collider, corresponding to an integrated luminosity of 140 fb^{-1}. No evidence of the signal is found and the observed (expected) upper limit on the cross-section for non-resonant Higgs boson pair production is determined to be 18 (11) times the Standard Model predicted cross-section at 95% confidence level.

ATLAS-CONF-2024-005
02 April 2024

Contents

1 Introduction

Since the discovery of the Higgs boson by the ATLAS and CMS Collaborations in 2012 [1, 2], a major focus in particle physics has been understanding how the Higgs boson interacts with other particles. Tremendous progress has been made in determining the strength of the Higgs boson's couplings to fermions and vector bosons, but its self-interaction has yet to be established. Measurements of the Higgs self-coupling are an essential component of understanding electroweak symmetry breaking and are a sensitive probe for new physics. The nature of the electroweak phase transition, when the electromagnetic and weak forces differentiated as the universe cooled down after the Big Bang is still unknown. The Standard Model (SM) predicts a smooth continuous cross-over from one phase to the other, but a first-order phase transition is needed in most models in order to accommodate phenomena like baryonic asymmetry with baryogenesis. New physics that interacts with the Higgs boson is required to accommodate the needed first-order phase transition, and this in turn leads to a large modification ($\mathcal{O}(1)$ times the SM prediction) to the Higgs

self-coupling [3–5]. Some inflation models require that the Higgs boson couples to gravity, which in turn modifies the shape of the Higgs potential. Measurements of the Higgs self-coupling can provide important information to constrain such models [6]. In addition to providing information about the formation of the universe, self-coupling measurements can also provide insight into its stability [7] and eventual fate.

The most natural way to probe the Higgs self-interaction is via searches for Higgs boson pair production, HH. At the LHC the dominant HH production mode in the SM is by gluon-fusion (ggF). The leading order (LO) Feynman diagrams for this process are shown in Figure 1. The ggF cross-section, for a Higgs boson mass of $m_H = 125\,\text{GeV}$, calculated at next-to-next-to-leading-order (NNLO) accuracy in the finite top-quark mass approximation, is $\sigma_{HH}(\text{ggF}) = 31.1^{+6.7\%}_{-23.2\%}$ [8–15]. The two ggF production modes shown in Figure 1 interfere with each other destructively in the SM. The cross-section of the $pp \to HH$ process and shape of the m_{HH} distribution changes as the strength of the Higgs self-coupling relative to the SM prediction (denoted as $\kappa_\lambda = \lambda_{HHH}/\lambda_{SM}$) is varied.

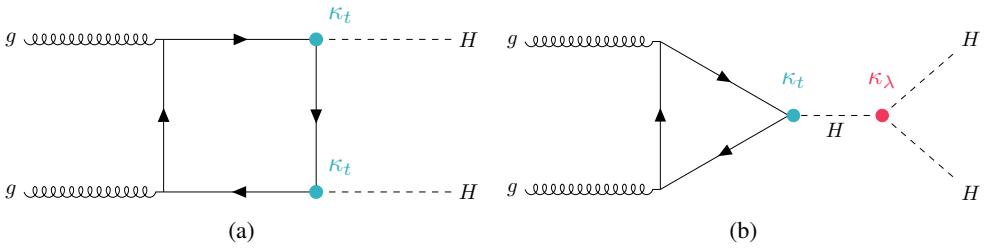

Figure 1: Leading order diagrams for gluon-fusion HH production, via (a) top box, and (b) the self-interaction 'triangle' modes.

The vector boson fusion (VBF) HH process provides a sub-leading source of HH production in the SM, and has a cross-section of $1.726 \pm 2.1\%$ fb, calculated at next-to-next-to-next-to-leading order (N^{3}LO) with $m_H = 125\,\text{GeV}$ [16–20]. The VBF production mode provides additional sensitivity to the Higgs self-coupling, as shown in Figure 2. Both the gluon-fusion and VBF production modes of Higgs boson pairs are considered as signal in this paper. Other production modes have lower cross-sections and are neglected.

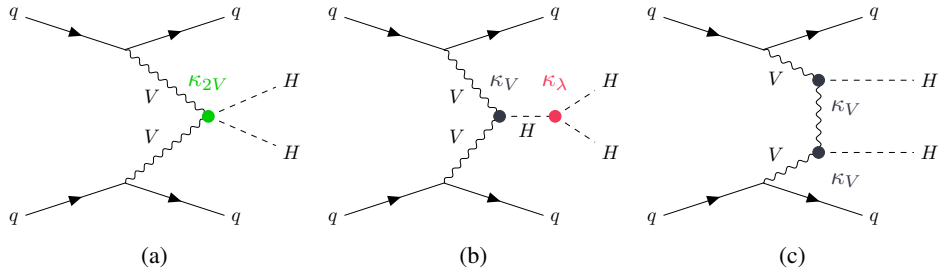

Figure 2: Leading order diagrams for VBF HH production.

HH production has been extensively explored by both the ATLAS and CMS experiments. A statistical combination of ATLAS results in the $HH \to bb\gamma\gamma$ [21], $HH \to bb\tau\tau$ [22], and $HH \to 4b$ [23] [1] channels using the full Run 2 dataset (up to $140\,\text{fb}^{-1}$ data collected during 2015–2018 with centre-of-mass energy $\sqrt{s} = 13$ TeV) sets an observed (expected) upper limit on the Higgs pair production cross-section at 2.4

[1] The notations $\tau\tau$, bb etc are used throughout in place of $\tau^+\tau^-$, $b\bar{b}$ etc, as charge conjugation is implied.

(2.9) times the SM prediction at 95% confidence level (CL) [24]. These results are further combined with precision measurements of single Higgs properties to constrain the self-coupling strength modifier to be within the range of $-0.4 \leq \kappa_\lambda \leq 6.3$ ($-1.9 \leq \kappa_\lambda \leq 7.6$ expected) at 95% CL. More recent results improve the performance of the individual $HH \to bb\gamma\gamma$ [25] and $HH \to bb\tau\tau$ [26] channels, and probe the HH process in final states with two b-jets, two light leptons ($\ell = e/\mu$) and missing transverse momentum ($E_{\mathrm{T}}^{\mathrm{miss}}$) [27], but the aforementioned combination continues to set the overall strongest limits on the HH cross-section and self-coupling strength.

The CMS Collaboration achieves similar sensitivity to the ATLAS results in a combination of results [28] from analysis of the $HH \to bb\gamma\gamma$ [29], $HH \to bb\tau\tau$ [30], $HH \to 4b$ [31, 32] and $HH \to bbZZ(ZZ \to 4\ell)$ [33] decay channels. A 'multilepton' analysis covering the $HH \to 4W$, $WW\tau\tau$, and 4τ decay modes in final states with two, three or four light leptons or hadronic taus [34] is also included in this combination. This multilepton analysis sets an observed (expected) upper limit on the cross-section of 21.3 (19.4) times the SM prediction and on the Higgs boson self-coupling strength of $-6.9 \leq \kappa_\lambda \leq 11.1$ ($-6.9 \leq \kappa_\lambda \leq 11.7$), all at 95% CL.

The analysis described in this paper provides a complementary way to probe Higgs boson pair production by targeting gluon-fusion production of the HH process in final states with multiple light leptons and hadronic taus, and in diphoton final states with up to two additional light leptons and/or hadronic taus. A visualisation of the final states covered in this analysis is shown in Figure 3. The analysis is designed to select events from HH decays where $H \to WW$, ZZ, $\tau\tau$, and $\gamma\gamma$. The $HH \to bbZZ$ decay mode, with both Z bosons decaying to light leptons, is also analysed in a dedicated search. Channels including an $H \to \gamma\gamma$ decay are classified as the diphoton plus multilepton channels ('$\gamma\gamma$+ML') while those without photons are classified as multilepton ('ML') channels. This is the first time these HH decay channels have been explored in a holistic way in ATLAS. The event selections are orthogonal by construction with those used in the ATLAS analyses of the $bb\gamma\gamma$ [21, 25], $bb\tau\tau$ [22, 26], and $bb\ell\ell + E_{\mathrm{T}}^{\mathrm{miss}}$ [27] HH decay channels. Boosted decision trees (BDTs) are used to enhance signal to background separation.

2 ATLAS detector

The ATLAS detector [35] at the LHC covers nearly the entire solid angle around the collision point.[2] It consists of an inner tracking detector surrounded by a thin superconducting solenoid, electromagnetic and hadron calorimeters, and a muon spectrometer incorporating three large superconducting air-core toroidal magnets.

The inner-detector system is immersed in a 2 T axial magnetic field and provides charged-particle tracking in the range $|\eta| < 2.5$. The high-granularity silicon pixel detector covers the vertex region and typically provides four measurements per track, the first hit normally being in the insertable B-layer (IBL) installed before Run 2 [36, 37]. It is followed by the silicon microstrip tracker (SCT), which usually provides eight measurements per track. These silicon detectors are complemented by the transition radiation tracker (TRT), which enables radially extended track reconstruction up to $|\eta| = 2.0$. The TRT also provides electron

[2] ATLAS uses a right-handed coordinate system with its origin at the nominal interaction point (IP) in the centre of the detector and the z-axis along the beam pipe. The x-axis points from the IP to the centre of the LHC ring, and the y-axis points upwards. Polar coordinates (r, ϕ) are used in the transverse plane, ϕ being the azimuthal angle around the z-axis. The pseudorapidity is defined in terms of the polar angle θ as $\eta = -\ln\tan(\theta/2)$ and is equal to the rapidity $y = \frac{1}{2}\ln\left(\frac{E+p_z c}{E-p_z c}\right)$ in the relativistic limit. Angular distance is measured in units of $\Delta R \equiv \sqrt{(\Delta y)^2 + (\Delta\phi)^2}$.

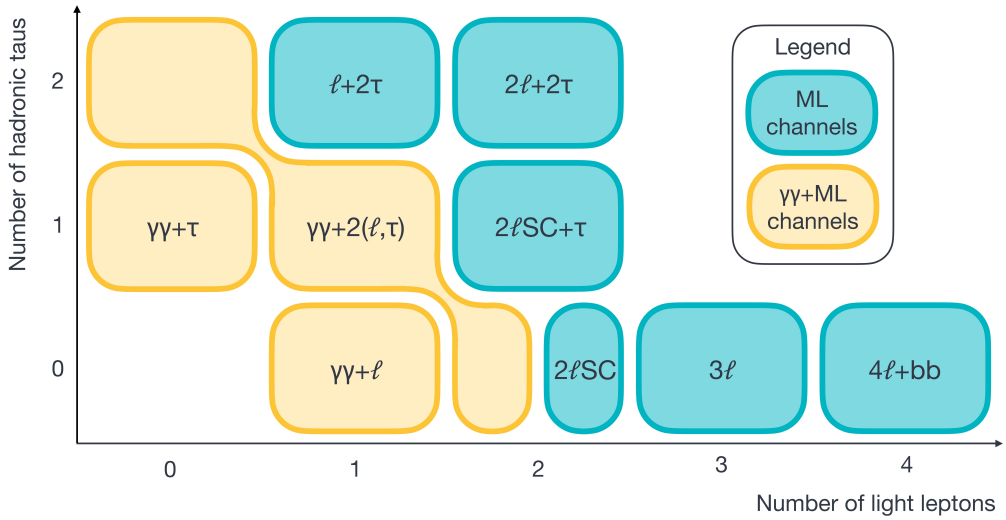

Figure 3: A visualisation of the different final states included in this analysis. The diphoton plus multilepton channels ('$\gamma\gamma$+ML channels') are shown in yellow boxes and channels with light leptons and hadronic taus ('ML channels') are indicated by turquoise boxes. 'SC' indicates that the two leptons are required to have the same-sign charge. The two hadronic taus in the 2ℓ+2τ and ℓ+2τ channels are required to have opposite-sign charge ('OC'), as are the two light leptons in the 2ℓ+2τ channel. The $\gamma\gamma$+$2(\ell,\tau)$ channel requires the presence of two light leptons or hadronic taus in addition to the two photons, i.e. encompassing $\gamma\gamma + \ell\ell$, $\gamma\gamma + \ell\tau$, and $\gamma\gamma + \tau\tau$ final states.

identification information based on the fraction of hits (typically 30 in total) above a higher energy-deposit threshold corresponding to transition radiation.

The calorimeter system covers the pseudorapidity range $|\eta| < 4.9$. Within the region $|\eta| < 3.2$, electromagnetic calorimetry is provided by barrel and endcap high-granularity lead/liquid-argon (LAr) calorimeters, with an additional thin LAr presampler covering $|\eta| < 1.8$ to correct for energy loss in material upstream of the calorimeters. Hadron calorimetry is provided by the steel/scintillator-tile calorimeter, segmented into three barrel structures within $|\eta| < 1.7$, and two copper/LAr hadron endcap calorimeters. The solid angle coverage is completed with forward copper/LAr and tungsten/LAr calorimeter modules optimised for electromagnetic and hadronic energy measurements respectively.

The muon spectrometer (MS) comprises separate trigger and high-precision tracking chambers measuring the deflection of muons in a magnetic field generated by the superconducting air-core toroidal magnets. The field integral of the toroids ranges between 2.0 and 6.0 T m across most of the detector. Three layers of precision chambers, each consisting of layers of monitored drift tubes, covers the region $|\eta| < 2.7$, complemented by cathode-strip chambers in the forward region, where the background is highest. The muon trigger system covers the range $|\eta| < 2.4$ with resistive-plate chambers in the barrel, and thin-gap chambers in the endcap regions.

Interesting events are selected by the first-level trigger system implemented in custom hardware, followed by selections made by algorithms implemented in software in the high-level trigger [38]. The first-level trigger accepts events from the 40 MHz bunch crossings at a rate below 100 kHz, which the high-level trigger further reduces in order to record events to disk at about 1 kHz.

An extensive software suite [39] is used in data simulation, in the reconstruction and analysis of real and simulated data, in detector operations, and in the trigger and data acquisition systems of the experiment.

3 Data and simulated samples

3.1 Data sample

The analysis is performed using proton-proton collision data with $\sqrt{s} = 13$ TeV collected during the LHC Run 2. The number of additional pp interactions per bunch crossing (pile-up) in this dataset ranges from about 8 to 70, with an average of 34. After applying data quality requirements [40] the full dataset has an integrated luminosity of $140.1 \pm 1.2\,\text{fb}^{-1}$ [41]. The trigger requirements are discussed in Section 5.

3.2 Simulated event samples

Monte Carlo (MC) simulation is used for the modelling of signal events, as well as most background processes. All generated events are processed through a simulation [42] of the ATLAS detector geometry and response using GEANT4 [43], and through the same reconstruction software as the data. Corrections are applied to the simulated events so that the particle candidates' selection efficiencies, energy scales and energy resolutions match those determined from data control samples. The samples of simulated events are normalised to the corresponding predicted cross-sections, computed to the highest order available in perturbation theory. The mass of the top quark and Higgs boson are set to $m_t = 172.5$ GeV and $m_H = 125$ GeV, respectively.

The effect of multiple interactions in the same and neighbouring bunch crossings (pile-up) was modelled by overlaying the simulated hard-scattering event with inelastic proton–proton (pp) events generated with PYTHIA 8.186 [44] using the NNPDF2.3LO set of parton distribution functions (PDF) [45] and the A3 set of tuned parameters [46]. The Monte Carlo (MC) events were weighted to reproduce the distribution of the average number of interactions per bunch crossing ($\langle\mu\rangle$) observed in the data. The $\langle\mu\rangle$ value in data was rescaled by a factor of 1.03 ± 0.04 to improve agreement between data and simulation in the visible inelastic proton–proton (pp) cross-section [47].

The SM ggF HH signal process is simulated using the POWHEG BOX v2 generator [48, 49] at NLO, including finite top-quark-mass effects [9], using the PDF4LHC15 [50] PDF set. Parton showers and hadronisation are simulated with PYTHIA 8.244 [51] with the A14 set of tuned parameters [52] and the NNPDF2.3LO PDF set [45]. In order to assess parton showering uncertainties, alternative ggF samples are generated using the POWHEG BOX v2 generator at NLO with the PDF4LHC15 PDF set, interfaced to HERWIG 7.1.6 [53] for parton showering and hadronisation using the HERWIG 7.1-default set of tuned parameters [54] and MMHT2014LO PDF set [55].

The SM VBF HH signal process is simulated using MADGRAPH 2.7.3 [56] at LO with the NNPDF3.0NLO PDF set [57], interfaced with PYTHIA 8.244 for parton showering and hadronisation using the A14 set of tuned parameters and NNPDF2.3LO PDF set. In order to assess parton showering uncertainties, alternative LO samples are generated using MADGRAPH 2.7.3 with the NNPDF3.0NLO PDF set, interfaced to HERWIG 7.2.1 with the HERWIG 7.1-default set of tuned parameters and MMHT2014LO PDF set for parton showering and hadronisation.

The dominant background process to the ML channels is diboson (VV) production, which is estimated from simulation and normalised to data in control regions. Background processes involving non-prompt leptons, leptons with a wrongly-assigned charge, or misidentified hadronic taus are also important backgrounds to these channels, and are estimated using data-driven methods, as described in Section 7. The 4ℓ+bb channel also has substantial contributions from top quark pair production ($t\bar{t}$), including in association with a Z boson ($t\bar{t}Z$), and Z boson production in association with jets (Z+jets). The '$\gamma\gamma$-continuum' is the dominant background to the $\gamma\gamma$+ML channels, where the components of this are $\gamma\gamma$ production in association with a vector boson ($V\gamma\gamma$), a top quark pair ($t\bar{t}\gamma\gamma$), or jets ($\gamma\gamma$+jets). MC simulations of these three processes are used when training BDTs to separate signal from background (as described in Section 6), while samples with $\gamma\gamma$ production in association with one or two jets are used to derive uncertainties on the background estimate, as described in Section 7.5. Single Higgs boson production is considered as a background process to all channels, and is significant for the 4ℓ+bb and $\gamma\gamma$+ML channels. Higgs boson production in association with a vector boson (VH) process is the dominant source of single Higgs backgrounds in most channels and contributes between 70% and 90% of the total single Higgs background in all channels except the $\gamma\gamma$+τ channel where it is approximately 50%, and the 4ℓ+bb channel where it is negligible. Gluon-fusion production is the dominant source of single Higgs production in the 4ℓ+bb channel, where it contributes around 50% of the single Higgs background. Higgs production in association with a top quark pair ($t\bar{t}H$) contributes between 7% and 30% of the total single Higgs background in all channels.

MC simulation samples are produced for the different signal and background processes using the configurations shown in Table 1. Details of the samples used to estimate the systematic uncertainties associated to the generators are shown in parentheses. All samples include leading-logarithm photon emission, either modelled by the parton shower generator or by Photos [58]. The Sherpa 2.2.4 [59] diphoton plus jets ($\gamma\gamma$+jets) sample is simulated with NLO-accurate matrix elements for up to one parton, and LO-accurate matrix elements for up to three partons are calculated with the Comix [60] and OpenLoops [61–63] libraries. Both the $\gamma\gamma$+jets and diphoton plus vector boson ($V\gamma\gamma$) samples are matched with the Sherpa parton shower [64] using the MEPS@NLO prescription [65–68] with a dynamic merging cut [69] of 10 GeV. Photons are required to be isolated according to a smooth-cone isolation criterion [70]. Samples are generated using the NNPDF3.0nnlo PDF set [57], along with the dedicated set of tuned parton-shower parameters developed by the Sherpa authors.

4 Object definitions

Vertices from pp interactions are reconstructed [79] using at least two inner detector tracks with $p_{\mathrm{T}} > 500$ MeV. In the ML channel analyses, the hard scatter primary vertex is defined to be the vertex with the largest sum of squared track momenta, $\sum p_{\mathrm{T}}^2$. For the $\gamma\gamma$+ML channel analyses, the hard scatter primary vertex is chosen using a neural network that uses information about inner detector tracks as well as the diphoton system [80].

Electrons, muons, hadronic taus, photons, jets (including those containing b-hadrons) and missing transverse energy, $E_{\mathrm{T}}^{\mathrm{miss}}$, are used in this search. Their reconstruction and identification are described below. Three selection definitions are used for both electrons and muons in the ML channel analyses–'Baseline', 'Loose', and 'Tight'–that are optimised for use in different channels and regions. A fourth definition is used in the $\gamma\gamma$+ML channels. The definitions are summarised in Table 2.

Table 1: The configurations used for event generation of signal and background processes. The samples used to estimate the systematic uncertainties are indicated in grey and enclosed in parentheses. V refers to production of an electroweak boson (W or Z/γ^*). The matrix element order refers to the order in the strong coupling constant of the perturbative calculation. Tune refers to the underlying-event tune of the parton shower generator. MG5_aMC refers to MadGraph5_aMC@NLO 2.2 or 2.3 [56]. MePs@Nlo refers to the method used in Sherpa to match the matrix element to the parton shower. Samples using Pythia 8 have heavy flavour hadron decays modelled by EvtGen 1.2.0 [71].

Process	Generator	ME order	Parton shower	PDF	Tune
Signal					
ggF HH	Powheg Box v2	NLO	Pythia 8	PDF4LHC15NLO	A14
	(Powheg Box v2)	(NLO)	(Herwig 7.1.6)	(MMHT2014lo)	(Herwig 7 default)
VBF HH	MG5_aMC	LO	Pythia 8	NNPDF3.0nlo	A14
	(MG5_aMC)	(LO)	(Herwig 7.0.4)	(MMHT2014lo)	Herwig 7 default
Top quark					
$t\bar{t}$	Powheg Box v2 [72–74]	NLO	Pythia 8	NNPDF3.0nlo	A14
	(Powheg Box v2)	(NLO)	(Herwig 7.1.3)	(NNPDF3.0nlo)	(H7-UE-MMHT)
$t\bar{t}t$	MG5_aMC	LO	Pythia 8	NNPDF2.3lo	A14
$t\bar{t}t\bar{t}$	MG5_aMC	NLO	Pythia 8	NNPDF3.1nlo	A14
	(Sherpa 2.2.10)	(NLO)	(Sherpa)	(NNPDF3.0nnlo)	(Sherpa default)
Single top (t-, Wt, s-channel)	Powheg Box v2 [75, 76]	NLO	Pythia 8	NNPDF3.0nlo	A14
$t\bar{t}W$	Sherpa 2.2.10	NLO	Sherpa	NNPDF3.0nnlo	Sherpa default
	(MG5_aMC)	(NLO)	(Pythia 8)	(NNPDF3.0nlo)	(A14)
tW,tZ/γ^*	MG5_aMC	NLO	Pythia 8	NNPDF2.3lo	A14
$t\bar{t}W^+W^-$	MG5_aMC	LO	Pythia 8	NNPDF2.3lo	A14
$t\bar{t}Z/\gamma^*(Z \to \ell^+\ell^-\gamma)$	MG5_aMC	NLO	Pythia 8	NNPDF3.0nlo	A14
tZ/γ^*	MG5_aMC	NLO	Pythia 8	NNPDF2.3lo	A14
Vector boson					
W+jets	Sherpa 2.2.1	NLO	Sherpa	NNPDF3.0nlo	Sherpa default
$Z \to \ell^+\ell^-\gamma$	Sherpa 2.2.1	NLO	Sherpa	NNPDF3.0nlo	Sherpa default
$Z \to \ell^+\ell^-\gamma$	Powheg Box v1	NLO	Pythia 8	CTEQ6L1nlo [77]	A14
$(\gamma^{(*)} \to e^+e^-)$	[48, 73, 74, 78]				
VV, $qqVV$,VVV	Sherpa 2.2.2	NLO	Sherpa	NNPDF3.0nnlo	Sherpa default
Photon					
$\gamma\gamma$+jets	Sherpa 2.2.4	NLO	MePs@Nlo	NNPDF3.0nnlo	Sherpa dedicated
$V\gamma\gamma$	Sherpa 2.2.4	LO	MePs@Nlo	NNPDF3.0nnlo	Sherpa dedicated
$t\bar{t}\gamma\gamma$	MG5_aMC	LO	Pythia 8	NNPDF2.3lo	A14
Single Higgs					
ggF H	Powheg	NLO	Pythia 8	PDF4LHC15 NNLO	AZNLO
VBF H	Powheg	NLO	Pythia 8	PDF4LHC15 NNLO	AZNLO
VH (inclusive)	Powheg Box	NLO	Pythia 8	NNPDF3.0nlo	A14
VH (W^+H, W^-H, $qq \to ZH$, $gg \to ZH$)	Powheg	NLO	Pythia 8	PDF4LHC15 NNLO	AZNLO
$t\bar{t}H$	Powheg Box v2	NLO	Pythia 8	NNPDF3.0nlo	A14
	(Powheg Box)	(NLO)	(Herwig 7.0.4)	(NNPDF3.0nlo)	(H7-UE-MMHT)
	(MG5_aMC)	(NLO)	(Pythia 8)	(NNPDF3.0nlo)	(A14)
$b\bar{b}H$	Powheg Box v2	NLO	Pythia 8	NNPDF3.0nlo	A14
tHb+jet(s)	MG5_aMC	NLO	Pythia 8	NNPDF3.0nlo	A14
tHW	MG5_aMC	NLO	Pythia 8	NNPDF3.0nlo	A14

Electrons are reconstructed and identified by matching inner detector tracks to energy deposits measured in the EM calorimeter [81]. Electron candidates are required to have $p_{\mathrm{T}} > 10\,\mathrm{GeV}$ and $|\eta| < 2.47$, excluding the calorimeter transition region $1.37 < |\eta| < 1.52$. The minimum p_{T} requirement is lowered to 4.5 GeV in the 4ℓ+bb channel, where one of the Z bosons is produced off-shell and as such its decay products are typically produced with low p_{T}. Electron candidates are identified using a likelihood technique and Baseline and Loose candidates are required to pass a loose identification working point, which, in combination with additional track hit requirements applied to ensure that the track is high quality, provides an overall electron selection efficiency of 95% in a $Z \to e^+e^-$ sample [81]. Tight electrons are required to pass a tight identification working point. No isolation requirements are applied as part of the Baseline definition, but Loose (Tight) electrons are required to pass loose (tight) isolation working points of a 'Prompt Lepton Veto' (PLV) BDT designed to reject non-prompt electrons [82]. Several signal regions are defined based on the relative charge of two leptons, so a charge (Q) mis-ID BDT is used to reject electron candidates where the charge is likely to have been wrongly attributed. The chosen working point provides a factor of 17 rejection of electron candidates with a wrongly-assigned charge for a 95% signal efficiency [81, 82] in $Z \to e^+e^-$ events. Contributions from converted photons are rejected using an ambiguity solving algorithm based on track information [81, 82]. A fourth electron definition working point is used in the $\gamma\gamma$+ML channels, where the electron candidates are required to have $p_{\mathrm{T}} > 10\,\mathrm{GeV}$, and pass the medium working point of the likelihood based identification. Isolation requirements are applied, based on the presence of tracks in a cone of p_{T}-dependent size around the electron and of calorimetric energy deposits in a fixed-size cone.

Muon candidates are reconstructed from tracks in the MS, that are matched to inner detector tracks where available. Baseline muon candidates are required to have $p_{\mathrm{T}} > 10\,\mathrm{GeV}$ and $|\eta| < 2.5$. The minimum p_{T} requirement is lowered to 3 GeV in the 4ℓ+bb channel in order to increase acceptance of muons from the decay of an off-shell Z boson. Baseline and Loose muons are required to pass a loose identification working point, and this is tightened to medium identification for the Tight muon definition [83]. Similarly to electrons, Loose and Tight muons are required to pass correspondingly strict working points of the PLV [83]. Muons used in the $\gamma\gamma$+ML channels are required to have $p_{\mathrm{T}} > 10\,\mathrm{GeV}$, pass a medium identification working point, and loose isolation requirements that are based on the presence of particle-flow objects [84] in a cone of p_{T}-dependent size around the muon.

To further reduce contributions from non-prompt electrons and muons, cuts on the transverse and longitudinal impact parameters, $|d_0|$ and $|z_0|$ respectively, are applied to all candidates. Electrons (muons) are required to have $|d_0|/\sigma_{d_0} < 5(3)$ and $|z_0 \sin\theta| < 0.5$ mm (where θ is the polar angle of the track).

The visible hadronic tau decay ($\tau_{\text{had-vis}}$) reconstruction algorithm [85] is seeded from jets formed using the anti-k_t algorithm [86, 87] with a radius parameter $R = 0.4$, and clusters of calorimeter cells calibrated using a local hadronic calibration (LC) [88] as inputs. The $\tau_{\text{had-vis}}$ candidates are required to have $p_{\mathrm{T}} > 20\,\mathrm{GeV}$ and $|\eta| < 2.5$. The calorimeter transition region ($1.37 < |\eta| < 1.52$) is vetoed. A set of BDTs are used to determine whether tracks in a cone with radius $R = 0.4$ around the $\tau_{\text{had-vis}}$ axis are consistent with coming from a hadronic tau decay. Selected $\tau_{\text{had-vis}}$ candidates are required to have either one or three associated tracks (or 'prongs'), with a total charge of ± 1. Recurrent neural networks (RNNs) are used to identify $\tau_{\text{had-vis}}$ candidates and reject backgrounds [89]. A loose identification working point is used in the $\gamma\gamma$+ML channels, providing an efficiency of 85% (75%) for one-prong (three-prong) $\tau_{\text{had-vis}}$. In the ML channels, the medium working point is used that has an efficiency of 75% (60%) for one-prong (three-prong) $\tau_{\text{had-vis}}$. A separate BDT is used to reject electrons that are misidentified as one-prong $\tau_{\text{had-vis}}$ candidates, with an efficiency of about 95% for real hadronic taus [85].

Anti-$\tau_{\text{had-vis}}$ objects, defined as a $\tau_{\text{had-vis}}$ with modified identification requirements, are used to estimate the backgrounds from jets misidentified as $\tau_{\text{had-vis}}$ in the 2ℓ+2τ and ℓ+2τ channels, as described in Section 7.4.

Table 2: Electron and muon candidate definitions used in the analysis. A '-' indicates that a cut is not applied, and 'N/A' indicates that a requirement is not applicable.

	Electrons				Muons			
	Baseline (B)	Loose (L)	Tight (T)	$\gamma\gamma$+ML (P)	Baseline (B)	Loose (L)	Tight (T)	$\gamma\gamma$+ML (P)
Minimum p_{T}	10 GeV (4ℓ+bb channel: 4.5 GeV)				10 GeV (4ℓ+bb channel: 3 GeV)			
η	$\lvert\eta\rvert < 1.37$ or $1.52 < \lvert\eta\rvert < 2.47$				$\lvert\eta\rvert < 2.5$			
Identification	Loose		Tight	Medium	Loose		Medium	
Isolation	-	PLV loose	PLV tight	Loose	-	PLV loose	PLV tight	Loose
Q mis-ID BDT	-	✓		-	N/A			
e/γ ambiguity	-	✓		-	N/A			
$\lvert d_0\rvert/\sigma_{d_0}$	< 5				< 3			
$\lvert z_0 \sin\theta\rvert$	< 0.5 mm				< 0.5 mm			

Anti-$\tau_{\text{had-vis}}$ objects are reconstructed, and their energy is calibrated in the same way as for $\tau_{\text{had-vis}}$ candidates, and they must satisfy the nominal $\tau_{\text{had-vis}}$ kinematic and track selection criteria. They are required to pass a very loose RNN identification requirement, corresponding to an efficiency of approximately 99% for $\tau_{\text{had-vis}}$ [89], but to fail the nominal RNN requirement applied to the $\tau_{\text{had-vis}}$ candidates.

Photon candidates are required to have $E_{\mathrm{T}} > 25$ GeV and $|\eta| < 2.37$. Photons inside the crack region of the calorimeter ($1.37 < |\eta| < 1.52$) are rejected. Photon identification is based on the lateral shower profile of the energy deposits in the first and second electromagnetic calorimeter layers and on the energy leakage fraction in the hadronic calorimeter. The photon candidates are also required to pass a tight working point of this identification algorithm, that is tuned for converted and unconverted photons separately [81]. Loose isolation requirements, based on calorimeter clusters and tracks in a cone with radius $R = 0.2$ around the photon are also applied [81]. For isolated photons with p_{T} between 30 GeV and 250 GeV, the identification efficiency for unconverted and converted photons ranges from 84% to 98%, when evaluated on a sample of $Z \to \ell^+\ell^-\gamma$ events [81].

Reconstructed jets are based on particle-flow objects built from noise-suppressed positive-energy topological clusters in the calorimeter and reconstructed tracks [84]. The anti-κ_t algorithm [86, 87] with a radius parameter of $R = 0.4$ is used. Jets are required to have rapidity $|y| < 4.4$ and $p_{\mathrm{T}} > 25$ GeV. To further suppress jets produced in concurrent pp interactions, each jet within the tracking acceptance of $|\eta| < 2.4$, and with $p_{\mathrm{T}} < 60$ GeV, is required to satisfy the tight jet-vertex tagger [90] criteria used to identify the jet as originating from the selected primary vertex of the event.

Jets containing b-hadrons, b-jets, are identified using a deep-learning neural network, DL1r [91] that combines information about the impact parameters of inner detector tracks, the presence of displaced secondary vertices, and reconstructed flight-paths of b- and c-hadrons inside the jet. Jets with $|\eta| < 2.5$ are considered for b-tagging. A working point that gives 77% efficiency to identify jets associated with a b-hadron in simulated $t\bar{t}$ events is used to select, or veto, b-jets. At this working point, the light-jet (charm-jet) rejection measured in $t\bar{t}$ simulation is about a factor of 130 (4.9) [92]. The DL1r algorithm is calibrated using a likelihood-based method for each jet type [92], and correction factors are applied to the simulated event samples to compensate for differences between data and simulation in the b-tagging efficiency for b-, c- and light-flavour jets. The energy of b-tagged jets is corrected for the possible contribution of muons from semileptonic b-hadron decays. In addition, the undetected energy of the

neutrinos and out-of-cone effects are corrected for with scale factors derived as a function of the b-jet p_{T} from a $t\bar{t}$ MC sample. The two corrections together improve the resolution of the invariant mass of the two jets with the highest b-tagging score (m_{bb}) by about 20% for non-resonant HH signal events that include a $H \to b\bar{b}$ decay. The procedure closely follows the one used in Ref. [93].

An overlap-removal procedure is applied in order to resolve ambiguities between independently reconstructed electrons, muons, (anti-)$\tau_{\text{had-vis}}$, photons and jets. Any electron found to share a track with a muon is removed, as is any (anti-)$\tau_{\text{had-vis}}$ within $\Delta R < 0.2$ of an electron or muon. Jets found within $\Delta R < 0.2$ of an electon or (anti-)$\tau_{\text{had-vis}}$ are removed, and any jet with less than three tracks associated to it is removed if it is found to be within $\Delta R < 0.2$ of a muon. Any electron or muon found within $\Delta R < 0.4$ of surviving jets is removed. Photons are removed if they are found within $\Delta R < 0.4$ of an electron or muon. Jets found within $\Delta R < 0.4$ of a photon are removed. All requirements are applied sequentially. A similar procedure is applied for the $\gamma\gamma$+ML channels, but prioritising keeping photons. All electrons and muons that satisfy the 'Baseline' definition are considered as inputs to the overlap-removal procedure in the ML channels while the $\gamma\gamma$+ML channels use the definitions described in the text and denoted as type 'P' in Table 2. The difference in overlap-removal procedures means that the ML and $\gamma\gamma$+ML channels are not strictly orthogonal, but no signal or data events are found to pass the selection requirements of more than one channel.

The missing transverse energy $E_{\mathrm{T}}^{\mathrm{miss}}$ in an event is calculated as the magnitude of the negative vectorial sum of the transverse momenta of all selected and calibrated physics objects that can be matched to the primary vertex, after the overlap procedure has been applied. A component called the "soft term" is calculated from the residual tracks that originate from the primary vertex but are not associated with any other object and is included in the calculation [94].

5 Event categorisation and preselection

Events in the ML channels that have final states containing two or more light leptons are selected by requiring that they pass single lepton or dilepton triggers [95, 96]. Events in the ℓ+2τ channel are selected using only the single lepton triggers. The single electron (muon) triggers have p_{T} thresholds of 24–26 GeV (20–26 GeV), depending on the data-taking conditions. The dilepton triggers require either two electrons, two muons, or one electron and one muon, and have p_{T} thresholds as low as 12 GeV (8 GeV) for the leading (subleading) lepton. Diphoton triggers [95] where the leading (subleading) photon is required to have $E_{\mathrm{T}} > 35$ GeV (25 GeV) are used in the $\gamma\gamma$+ML channels. The diphoton triggers used in 2015 and 2016 required both photons to satisfy the loose photon identification critera, and this was tightened to a medium identification working point during 2017-2018 data taking in response to the increased pp interaction rate. In all channels, the electrons, muons and photons are reconstructed offline are required to be geometrically matched to the object that fired the corresponding trigger.

Events are categorised into sub-channels according to the number of photons, $\tau_{\text{had-vis}}$, and light leptons passing the definitions in Table 2, after the overlap removal procedure has been applied. The requirements for the different sub-channels are summarised for the ML channels in Table 3 and for the $\gamma\gamma$+ML channels in Table 4. These sets of requirements define the signal preselection regions which are used for further multivariate analysis selections used to refine the extraction of signal as described in Section 6. The requirements also form the basis from which control and validation regions are defined in order to estimate background contributions, as described in Section 7. The contributions of the different decay modes of the

Higgs boson pair to different signal regions after applying the preselection requirements is shown for the ML channels in Figure 4 and for the $\gamma\gamma$+ML channels in Figure 5.

Table 3: Selection criteria applied to each ML channel to form the signal preselection regions. The notation 'Nℓ(X)' refers to the multiplicity, N, of the different types of lepton (X = B,L,T) as defined in Table 2. The multiplicity of $\tau_{\text{had-vis}}$, jets, and b-jets are denoted N_τ, N_{jet}, and $N_{b\text{-jet}}$, respectively. When no p_{T} (or E_{T}) threshold is specified, the default requirements for each object are used, as described in Section 4. Objects are ordered by decreasing p_{T} and their index denoted with a subscript. In the 4ℓ+bb channel, the SFOC lepton pair with an invariant mass closest to the Z-boson mass is defined as the lepton pair coming from the on-shell Z-boson decay (on-shell-$\ell\ell$) while the remaining SFOC lepton pair is defined as coming from the off-shell Z decay (off-shell-$\ell\ell$). In the 3ℓ channel, the lepton with opposite charge with respect to the other two is denoted as ℓ_{OC}. The remaining lepton that is nearest to ℓ_{OC} in ΔR is denoted ℓ_{SC1} and the remaining lepton is denoted ℓ_{SC2}. The 'Z-veto' requires that the invariant mass of two SFOC leptons must satisfy $|m_{\ell\ell} - m_Z| > 10\,\text{GeV}$. An analagous Z-veto requirement is considered for the three-lepton system in the 3ℓ channel in order to remove background processes with $Z \to \ell\ell\gamma^*(\gamma^* \to \ell'\ell')$ where one lepton has very low momentum and is not reconstructed.

Channel	ℓ	$\tau_{\text{had-vis}}$	Jets	b-jets
4ℓ+bb	4ℓ(B) $p_{\text{T}}(\ell_1) > 20\,\text{GeV}$ $p_{\text{T}}(\ell_2) > 15\,\text{GeV}$ $p_{\text{T}}(\ell_3) > 10\,\text{GeV}$ ℓ_3 or ℓ_4 pass loose PLV 2 SFOC pairs $50 < m^{\text{SFOC}}_{\text{on-shell-}\ell\ell} < 106\,\text{GeV}$ $5 < m^{\text{SFOC}}_{\text{off-shell-}\ell\ell} < 115\,\text{GeV}$ All 4 pairs $\Delta R(\ell_i, \ell_j) > 0.02$ $115\,\text{GeV} < m_{4\ell} < 135\,\text{GeV}$	$N_\tau = 0$	$N_{\text{jet}} \geq 2$	$1 \leq N_{b\text{-jet}} \leq 3$
3ℓ	3ℓ, sum of charges = ± 1 ℓ_{OC}(L) ℓ_{SC1}(T), $p_{\text{T}} > 15\,\text{GeV}$ ℓ_{SC2}(T), $p_{\text{T}} > 15\,\text{GeV}$ All $m^{\text{SFOC}}_{\ell\ell} > 12\,\text{GeV}$ Z-veto $\lvert m_{3\ell} - m_Z \rvert > 10\,\text{GeV}$	$N_\tau = 0$	$N_{\text{jet}} \geq 1$	$N_{b\text{-jet}} = 0$
2ℓSC	2ℓ(T), $p_{\text{T}} > 20\,\text{GeV}$, SC $m_{\ell\ell} > 12\,\text{GeV}$	$N_\tau = 0$	$N_{\text{jet}} \geq 2$	$N_{b\text{-jet}} = 0$
2ℓSC+τ	2ℓ(T), $p_{\text{T}} > 20\,\text{GeV}$, SC $m_{\ell\ell} > 12\,\text{GeV}$	$N_\tau = 1$ $p_{\text{T}} > 25\,\text{GeV}$ OC to ℓ	$N_{\text{jet}} \geq 2$	$N_{b\text{-jet}} = 0$
2ℓ+2τ	2ℓ(L), OC $m_{\ell\ell} > 12\,\text{GeV}$ Z-veto	$N_\tau = 2$, OC $\Delta R(\tau_1, \tau_2) < 2$	-	$N_{b\text{-jet}} = 0$
ℓ+2τ	1ℓ(L)	$N_\tau = 2$, OC $\Delta R(\tau_1, \tau_2) < 2$	$N_{\text{jet}} \geq 2$	$N_{b\text{-jet}} = 0$

Table 4: Selection criteria applied to each $\gamma\gamma$+ML channel to form the signal preselection regions. The notation '$N_{\ell(\mathrm{P})}$' refers to the multiplicity, N, of P-type leptons as defined in Table 2. The multiplicity of $\tau_{\text{had-vis}}$, photons, and b-jets are denoted N_τ, N_γ, and $N_{b\text{-jet}}$, respectively. When no p_T or E_T threshold is specified, the default requirements for each object are used, as described in Section 4. Photons are ordered in decreasing E_T and their index denoted with a subscript. The invariant masses of dilepton and diphoton systems are denoted $m_{2(\ell,\tau)}$ and $m_{\gamma\gamma}$ respectively.

Channel	ℓ	$\tau_{\text{had-vis}}$	Photons	$E_\mathrm{T}^{\text{miss}}$	b-jets
$\gamma\gamma$+2(ℓ,τ)	$N_{\ell(\mathrm{P})} + N_\tau = 2$, OC $m_{2(\ell,\tau)} > 12$ GeV		$N_\gamma = 2$ $E_\mathrm{T}(\gamma_1) > 35$ GeV 105 GeV $< m_{\gamma\gamma} <$ 160 GeV $\gamma_1 : p_\mathrm{T}/m_{\gamma\gamma} > 0.35$ $\gamma_2 : p_\mathrm{T}/m_{\gamma\gamma} > 0.25$	$E_\mathrm{T}^{\text{miss}} > 35$ GeV	$N_{b\text{-jet}} = 0$
$\gamma\gamma$+ℓ	$N_{\ell(P)} = 1$	$N_\tau = 0$		$\gamma\gamma$+e: $E_\mathrm{T}^{\text{miss}} > 35$ GeV $\gamma\gamma$+μ: -	
$\gamma\gamma$+τ	$N_{\ell(P)} = 0$	$N_\tau = 1$		$E_\mathrm{T}^{\text{miss}} > 35$ GeV	

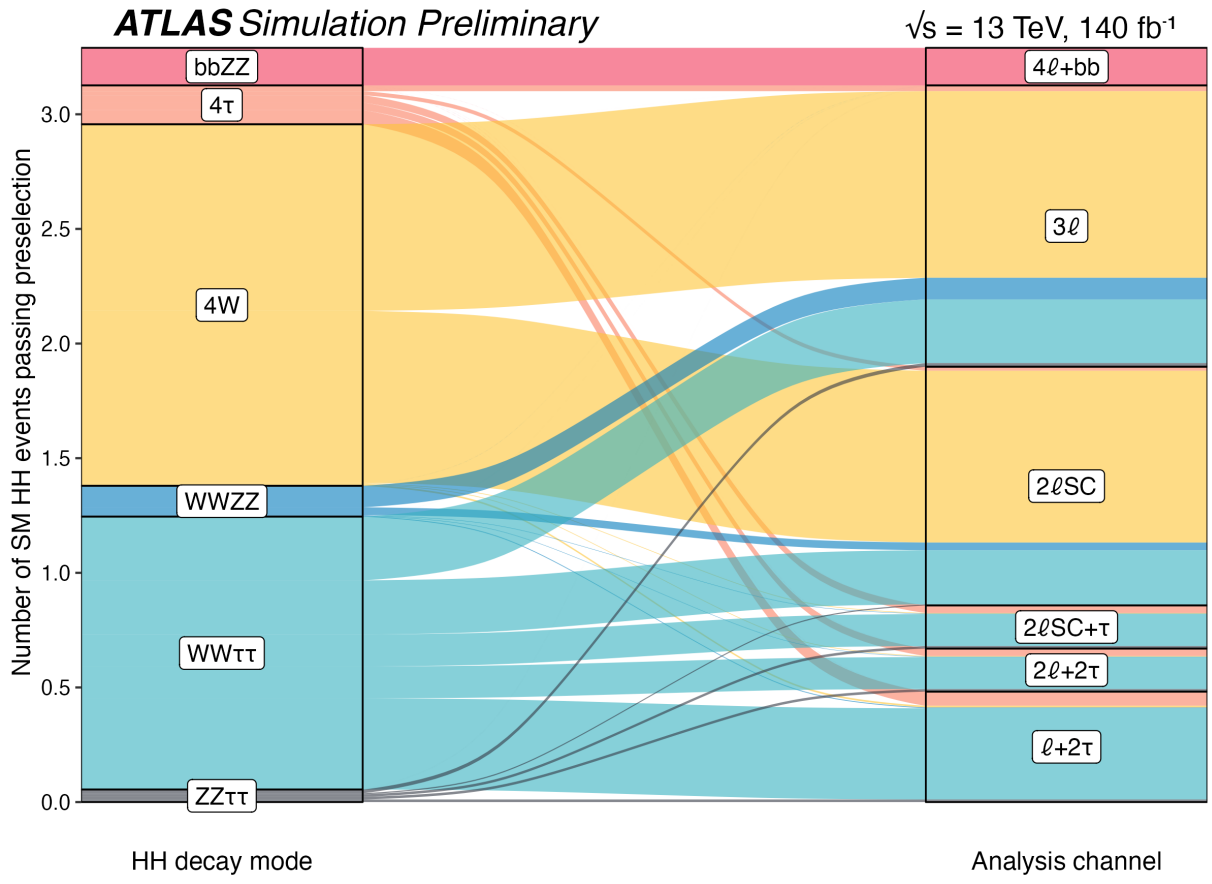

Figure 4: Number of ggF and VBF SM HH signal events passing the preselection requirements from the targeted HH decay modes on the left and their acceptance into the different ML search channels on the right. The $HH \to 4Z$ decay mode contributes less than 0.1% of preselected HH events and is not shown. The notation 'τ' denotes inclusive taus when refering to the Higgs decay mode (left), and hadronic taus when refering to the analysed decay channel (right).

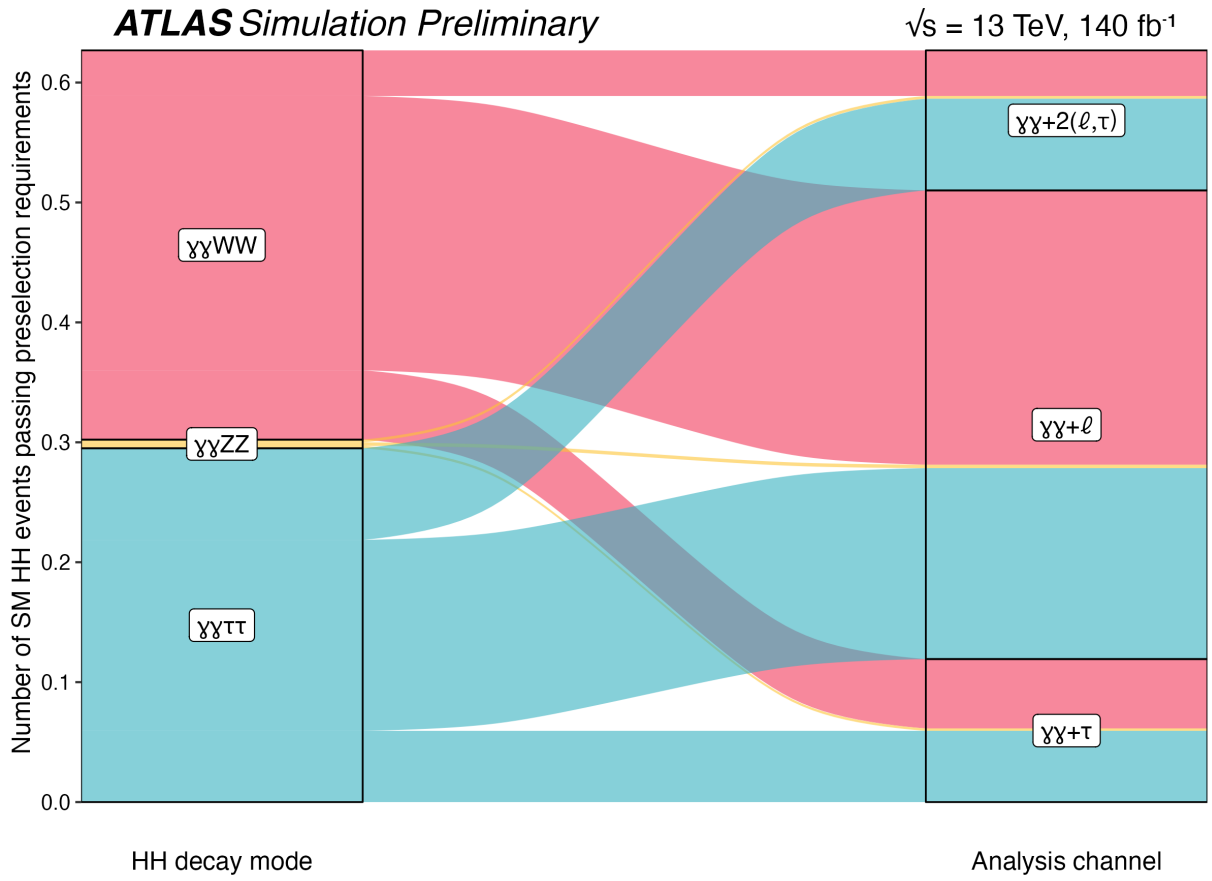

Figure 5: Number of ggF and VBF SM HH signal events passing the preselection requirements from the targeted HH decay modes on the left and their acceptance into the different $\gamma\gamma$+ML search channels on the right. The notation 'τ' denotes inclusive taus when refering to the Higgs decay mode (left), and hadronic taus when refering to the analysed decay channel (right).

6 Search strategy

All channels except the $\gamma\gamma$+2(ℓ,τ) channel use BDTs using the Gradient Boost [97] algorithm to separate signal from background processes. BDTs are optimised separately for each channel, in terms of the input variables and hyperparameters, using the area under the receiver operating characteristic (ROC) curve as the performance metric. Information about the kinematics of objects in the event are used as inputs to the BDT, as well as variables that probe the kinematic relationships between the objects, for example the angular separation or invariant mass of two or more objects. The most discriminating variables are: the p_{T} of the leading lepton (4ℓ+bb channel); the ΔR between the leading and sub-leading leptons (3ℓ and 2ℓSC+τ channels); the mimimum separation in R found between any lepton and any jet (2ℓSC channel); the invariant mass of the two leptons (2ℓ+2τ channel); the invariant mass of the leading lepton and the closest jet in ΔR (ℓ+2τ channel); and the p_{T} of the $H \to \gamma\gamma$ system ($\gamma\gamma$+ℓ and $\gamma\gamma$+τ channels). The complete list of all the variables used as inputs to the BDTs in the different channels is provided in the Appendix. No BDT or further event selection is used in the $\gamma\gamma$+2(ℓ,τ) channel analysis due to the low event yields and the signal region is therefore defined by the preselection requirements described in Section 5. Both the

ggF HH and VBF HH processes are considered as signal in all channels. All background processes are included when training the BDTs used for the 4ℓ+bb, 3ℓ, and $\gamma\gamma$+ML channel analyses, while the ML channels with hadronic taus in the final state (the 2ℓSC+τ, 2ℓ+2τ and ℓ+2τ channels) are trained only against the dominant diboson (VV) background process. For the 2ℓSC channel, better separation of signal from background was demonstrated by training three BDTs separately to distinguish the HH signal from the main VV, $t\bar{t}$, and Z+jets background processes. The three output BDT score distributions are then used as the input variables to a fourth BDT which is used as the final discriminating variable to separate signal from background. This strategy was found to improve the sensitivity of the 2ℓSC channel over the use of a single-BDT approach by providing a better handle to discriminate against the three major backgrounds.

The BDT output score distribution is used as the final discriminant in each of the ML channels. The full distribution is used in the 4ℓ+bb, 2ℓ+2τ, and ℓ+2τ channels, while the 3ℓ, 2ℓSC, and 2ℓSC+τ channels use the high-BDT-score region as the signal region, and use the low-BDT-score region to validate the background model or constrain background processes, as described in Section 7. The BDT output score in the signal region is shown for each channel in Figure 6. In the $\gamma\gamma$+ℓ and $\gamma\gamma$+τ channels the BDT score is used to define 'Tight' (0.6 < BDT score ≤ 1), 'Medium' (0 < BDT score ≤ 0.6) and 'Loose' ($-1 \leq$ BDT score ≤ 0) signal regions, where the Loose BDT score regions are used primarily as a background control region in the fit. The $m_{\gamma\gamma}$ distribution is used as the final discriminant in each $\gamma\gamma$+ML signal region, as shown in Figure 7. The distributions in Figures 6 and 7 are shown after applying the likelihood fit to data (i.e. 'post-fit') under the background-only hypothesis as described in Section 9.

7 Background estimation

The background composition varies for the different channels. Processes where the event selection requirements described in Section 5 are satisified by prompt leptons and real hadronic taus produced in the decay chain are estimated using MC simulations (described in Section 3.2). Of these, the dominant background processes are normalised using control regions (CRs) in data that are orthogonal to the signal regions. The normalisation factors obtained in the CRs are then applied to the simulated events in the signal region. Contributions from processes where at least one of the candidate leptons is a non-prompt lepton from b-hadron decays or photon conversions, or a lepton with misidentified charge, are estimated using data-driven techniques. Jets misidentified as $\tau_{\text{had-vis}}$ are referred to as fake-τ_{had} and are also estimated from data, as is the non-resonant $\gamma\gamma$ processes that make up the dominant background to the $\gamma\gamma$+ML channel analyses. All ML channels employ a validation region (VR) that is used to verify the background modelling outside of the signal region and good agreement between data and the background predictions is observed throughout. The requirements that are applied to define the various control and validation regions, relative to the preselection requirements defined in Section 5, are shown in Table 5 for channels without $\tau_{\text{had-vis}}$, and Table 6 for channels with $\tau_{\text{had-vis}}$. Details about how the different types of background processes are estimated are given below. The evaluation of the systematic uncertainties associated to the (semi-)data-driven background is also described. Theoretical uncertainties on MC simulations are detailed in Section 8.2.

7.1 Prompt leptons

Diboson processes are a major background process to all of the ML channels, particularly the 3ℓ, 2ℓSC, and 2ℓSC+τ channels where these constitute approximately half the total background. A CR requiring

Table 5: Selection criteria applied to form the control and validation regions used to estimate backgrounds, for the 4ℓ+bb, 3ℓ, and 2ℓSC channels with respect to those used to define the preselection regions in Table 3. Requirements that are unchanged with respect to the preselection region are not listed (and indicated with a '-' if completely unchanged for a given type of object). The multiplicity of jets, and b-jets are denoted N_{jet} and $N_{b\text{-jet}}$, respectively. When no p_{T} (or E_{T}) threshold is specified, the default requirements for each object are used, as described in Section 4. Same-charge (opposite-charge) requirements between objects are denoted as 'SC' ('OC'). The notation 'SF' is used to indicate where leptons are required to have the same flavour. SFOC stands for same-flavour, opposite-charge. The 'Z-veto' requires that the invariant mass of two SFOC leptons must satisfy $|m_{\ell\ell} - m_Z| > 10\,\text{GeV}$, while '$Z$-req.' inverts this selection. In the 4ℓ+bb channel, the SFOC lepton pair with an invariant mass closest to the Z-boson mass is defined as the lepton pair coming from the on-shell Z-boson decay (on-shell-$\ell\ell$) while the remaining SFOC lepton pair is defined as coming from the off-shell Z decay (off-shell-$\ell\ell$). Regions that are included in the final fit are indicated with a *.

Channel	Region	Leptons	Jets	b-jets	Additional selections
4ℓ+bb	$t\bar{t}$ CR*	Off-shell-$\ell\ell$ not SFOC Z-veto	-	-	-
	$t\bar{t}Z$ CR*	Off-shell-$\ell\ell$ not SFOC All ℓ pass loose PLV Z-req. $m_{4\ell}$ req. removed	-	-	-
	VV, H CR*	All ℓ pass loose PLV	-	$N_{b\text{-jet}} = 0$	-
	Z+jets CR*	$p_{\text{T}}(\ell_3) < 10\,\text{GeV}$ $p_{\text{T}}(\ell_4) < 10\,\text{GeV}$ Z-req.		-	- -
	VR	-	-	-	$\lvert m_{4\ell} - m_H\rvert > 10\,\text{GeV}$
3ℓ	WZ CR	Z-req.	-	-	$E_{\text{T}}^{\text{miss}} > 30\,\text{GeV}$
	HF-e CR*	ℓ_{SC1}, ℓ_{SC2} both e No PLV on any ℓ	$N_{\text{jet}} \geq 2$	$N_{b\text{-jet}} \geq 2$	
	HF-μ CR*	ℓ_{SC1},ℓ_{SC2} both μ No PLV on any ℓ	$N_{\text{jet}} \geq 2$	$N_{b\text{-jet}} \geq 2$	
	Mat. conv. CR*	$\lvert m_{3\ell} - m_Z\rvert < 10\,\text{GeV}$ $r_{\text{vtx}} > 20\,\text{mm}$ $0 < m_{\text{trk,trk}} < 100\,\text{MeV}$	-	-	-
	VR	-	-	-	BDT $<$ 0.55
2ℓSC	WZ CR*	$\geq 3\ell$(T), $p_{\text{T}} > 20\,\text{GeV}$ One SFOC pair Z-req. $m_{\ell\ell}$ (any pair) $> 12\,\text{GeV}$ $\lvert m_{3\ell} - m_Z\rvert > 10\,\text{GeV}$	-	-	$E_{\text{T}}^{\text{miss}} > 30\,\text{GeV}$
	VVjj CR*	Z-veto (SFSC pair)	$m_{\text{jj}} > 300\,\text{GeV}$	-	BDT < -0.4 $\text{BDT}_{V\text{+jets}} > -0.8$
	HF-e CR1*	ℓ(T)e(T), no PLV	$2 \leq N_{\text{jet}} \leq 3$	$N_{b\text{-jet}} = 1$	-
	HF-e CR2*	ℓ(T)e(T), no PLV	$2 \leq N_{\text{jet}} \leq 3$	$N_{b\text{-jet}} \geq 2$	-
	HF-μ CR*	ℓ(T)μ(T), no PLV	$2 \leq N_{\text{jet}} \leq 3$	$N_{b\text{-jet}} \geq 1$	-
	Mat. conv. CR*	$r_{\text{vtx}} > 20\,\text{mm}$ $m_{\text{trk,trk}} < 100\,\text{MeV}$	-	-	-
	Int. conv. CR*	$r_{\text{vtx}} < 20\,\text{mm}$ $m_{\text{trk,trk}} < 100\,\text{MeV}$	-	-	-
	Q mis-ID	2e(T), OC or SC	$N_{\text{jet}} < 2$	-	-
	VR	-	-	-	BDT < -0.4

Table 6: Selection criteria applied to form the control and validation regions used to estimate backgrounds, for the 2ℓSC+τ, 2ℓ+2τ, and ℓ+2τ channels with respect to those used to define the preselection regions in Table 3. Requirements that are unchanged with respect to the preselection region are not listed (and indicated with a '-' if completely unchanged for a given type of object). The multiplicity of (anti-)$\tau_{\text{had-vis}}$, jets, and b-jets are denoted $N_{\text{anti-}\tau}$, N_{jet}, and $N_{b\text{-jet}}$, respectively. When no p_{T} (or E_{T}) threshold is specified, the default requirements for each object are used, as described in Section 4. Same-charge (opposite-charge) requirements between objects are denoted as 'SC' ('OC'). The notation 'SFOC' stands for same-flavour, opposite-charge. The 'Z-veto' requires that the invariant mass of two SFOC leptons must satisfy $|m_{\ell\ell} - m_Z| > 10$ GeV, while 'Z-req.' inverts this selection. Regions that are included in the final fit are indicated with a *. The 2ℓ+2τ and ℓ+2τ channels use the same regions of data to derive fake-factors in the Z+jets CR and $t\bar{t}$ VR, but are each defined here with respect to their own preselection requirements for completeness.

Channel	Region	Leptons	(anti-)$\tau_{\text{had-vis}}$	Jets	b-jets	Additional selections
2ℓSC+τ	VV CR*	-	-	-	-	BDT < -0.2
	HF-e CR1*	ℓ(T)e(T), no PLV	-	$N_{\text{jet}} \geq 2$	$N_{b\text{-jet}} = 1$	-
	HF-e CR2*	ℓ(T)e(T), no PLV	-	$N_{\text{jet}} \geq 2$	$N_{b\text{-jet}} \geq 2$	-
	HF-μ CR*	ℓ(T)μ(T), no PLV	-	-	-	-
	Fake-$\tau_{\text{had-vis}}$ CR	OC leptons Z-veto	-	-	-	-
	Z+jets VR	OC leptons Z-req.	-	-	-	-
	$t\bar{t}$ VR	OC leptons Z-veto	-	$N_{\text{jet}} = 2$	$N_{b\text{-jet}} = 1$	-
	VR	-	-	$N_{\text{jet}} < 2$	-	
2ℓ+2τ	Fake-$\tau_{\text{had-vis}}$ CR	-	$N_\tau = 1$ and $N_{\text{anti-}\tau} = 1$ or $N_{\text{anti-}\tau} = 2$		-	-
	Z+jets CR	Z-req.	$N_\tau \geq 1$ or $N_{\text{anti-}\tau} \geq 1$	-	-	-
	$t\bar{t}$ VR	-	$N_\tau \geq 1$ or $N_{\text{anti-}\tau} \geq 1$	-	$N_{b\text{-jet}} = 1$	-
	VR	-	SC $\tau_{\text{had-vis}}$	-	-	-
ℓ+2τ	Fake-$\tau_{\text{had-vis}}$ CR	-	$N_\tau = 1$ and $N_{\text{anti-}\tau} = 1$ or $N_{\text{anti-}\tau} = 2$		-	-
	Z+jets CR	2ℓ(T), OC Z-req.	$N_\tau \geq 1$ or $N_{\text{anti-}\tau} \geq 1$	-	-	-
	$t\bar{t}$ VR	2ℓ(T), OC Z-veto	$N_\tau \geq 1$ or $N_{\text{anti-}\tau} \geq 1$	-	$N_{b\text{-jet}} = 1$	-
	VR	-	SC $\tau_{\text{had-vis}}$	-	-	-

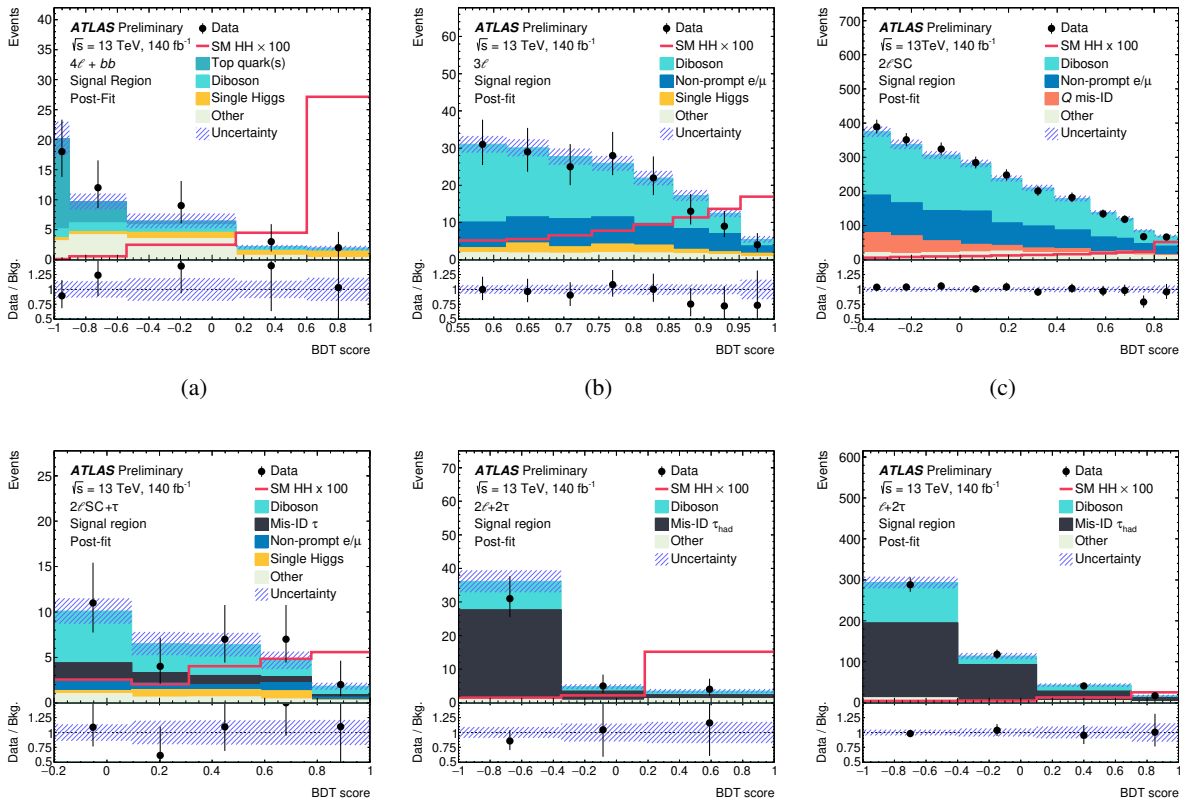

Figure 6: Distributions of the BDT output score in the signal regions of the (a) 4ℓ+bb, (b) 3ℓ, (c) 2ℓSC, (d) 2ℓSC+τ, (e) 2ℓ+2τ, and (f) ℓ+2τ channels, and applying the likelihood fit to data under the background-only hypothesis as described in Section 9. The SM HH signal scaled by a factor of 100 is also shown. The uncertainty bands include all sources of statistical and systematic uncertainties on the background prediction.

$E_{\mathrm{T}}^{\mathrm{miss}} > 30$ GeV and selecting events that contain a same-flavour, opposite charge pair of leptons with an invariant mass consistent with the Z boson mass, is used in the 3ℓ channel to provide a region enriched in WZ events. A polynomial function is fitted to the jet multiplicity distribution in the CR which is then applied to simulated WZ events in all other regions. The uncertainty in the reweighting is evaluated by varying the fit function parameters within their uncertainties and reevaluating the impact on the WZ process. Two CRs are employed in the 2ℓSC channel to normalise diboson processes, one enriched in WZ events (WZ CR) that follows closely the definition used for the equivalent CR in the 3ℓ channel, and the other targeting VV production in association with two or more jets (VVjj CR), that that controls the significant background from same-charge W boson pairs produced by vector boson scattering (VBS $W^{\pm}W^{\pm}$). The full definitions are provided in Table 5. The WZ CR corrects for mismodellings in the MC simulations for diboson events with large jet multiplicity [98], while the VVjj CR corrects for known mismodellings in the simulation of VBS processes [99]. A single bin in the WZ CR, and the H_{T} (scalar sum of the p_{T} of all jets) distribution in the VVjj CR, are included in the final fit. Normalisation factors of 0.80±0.05 and 1.60±0.13 are obtained for the WZ and VBS $W^{\pm}W^{\pm}$ processes, respectively. A low-BDT-score (< 0.2) region is used to constrain the VV background in the 2ℓSC+τ channel. This region is included in the final fit and a normalisation factor of 0.91 ± 0.23 is obtained.

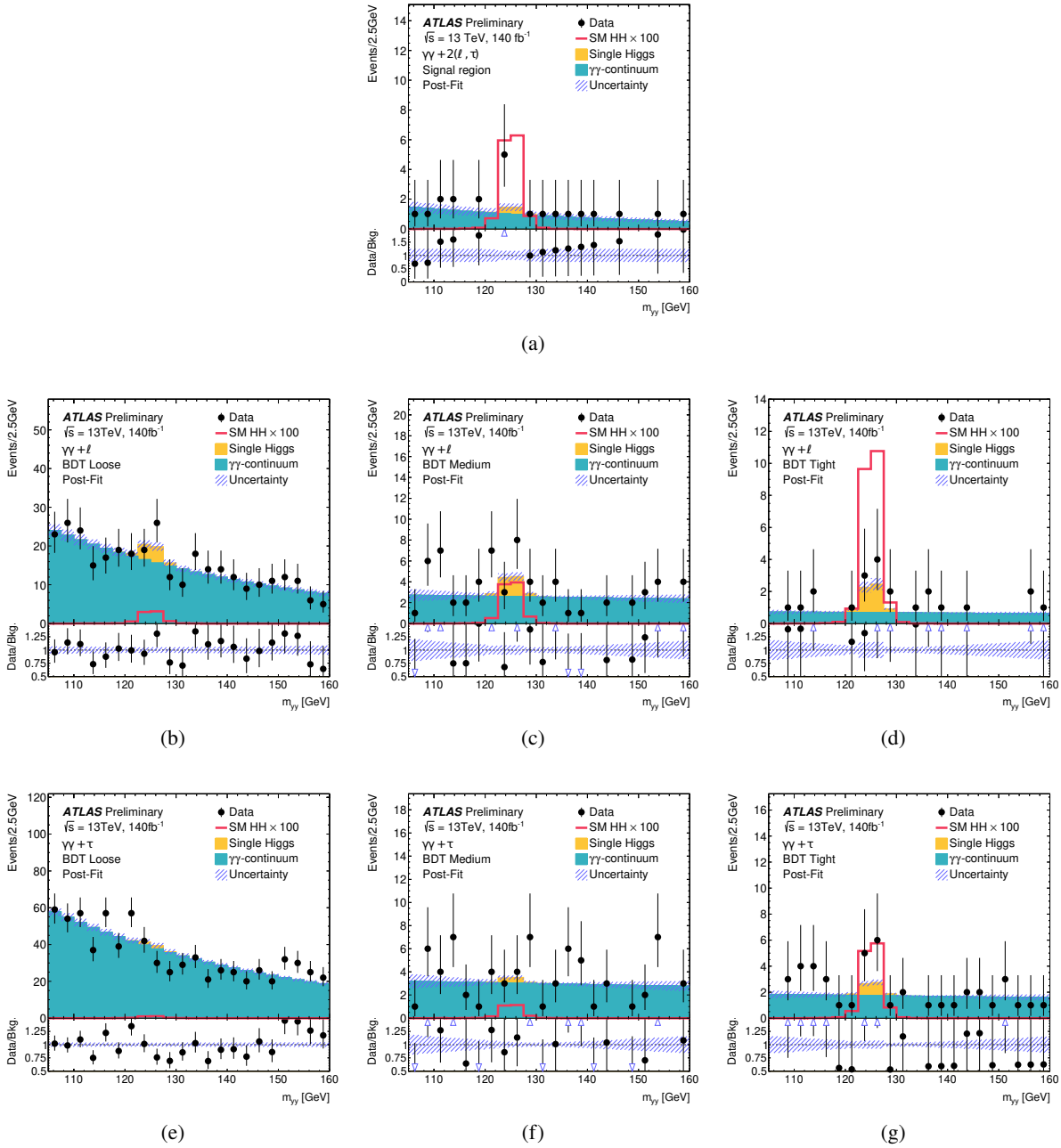

Figure 7: Distributions of the invariant mass of the diphoton system in the (a) $\gamma\gamma$+2(ℓ,τ), (b–d) $\gamma\gamma$+ℓ, and (e–g) $\gamma\gamma$+τ channels, after applying the selection requirements described in Section 5 and applying the likelihood fit to data under the background-only hypothesis as described in Section 9. The SM HH signal scaled by a factor of 100 times is also shown. The uncertainty bands include all sources of statistical and systematic uncertainties on the background prediction.

A CR requiring that there are no b-jets in the event and that all four leptons pass the isolation requirements is used in the 4ℓ+bb channel to simultaneously constrain the VV and single Higgs backgrounds in the fit. Normalisation factors of 1.12±0.46 and 1.09±0.42 are obtained. An additional 100% uncertainty on the normalisation of single Higgs processes produced via gluon-fusion, VBF or in association with a vector boson, is applied in the 4ℓ+bb channel, in order to account for difficulties in the modelling of these processes in association with heavy-flavour jets [100, 101]. Other CRs, defined in Table 5, are used in the 4ℓ+bb channel to constrain the $t\bar{t}Z$ (normalisation factor, $\mu = 1.27\pm0.22$), $t\bar{t}$ ($\mu = 1.50\pm0.28$) and Z+jets ($\mu = 1.01\pm0.36$) backgrounds. The latter two contain a mix of prompt and non-prompt or misidentified leptons but no attempt is made to separate these and the background shape is determined using MC simulations. The BDT classifier used to discriminate signal from background is applied to the data and simulated samples in the 4ℓ+bb channel CRs and the resulting BDT output score distributions are included in the final fit.

The normalisation of the $t\bar{t}W$ background to the 2ℓSC channel is obtained while performing the final fit by allowing the normalisation of the $t\bar{t}W$ process to float in the three CRs used to constrain the non-prompt lepton backgrounds from decays of heavy-flavour hadrons, as described below. The $t\bar{t}W$ process, that can yield a true same-charge lepton pair, provides a significant contribution in these CRs. A normalisation factor of 1.17±0.34 is obtained. For all other cases, background processes involving prompt leptons and real hadronic taus are taken directly from MC simulations and normalised to their cross-sections at the highest order available.

7.2 Non-prompt leptons

The non-prompt leptons background category encompasses events where lepton candidates do not originate from the primary interaction point. These non-prompt lepton backgrounds arise from various sources including $t\bar{t}$, Z+jets, W+jets, $V\gamma$, and other processes where a lepton is produced from a heavy-flavour (b, c) hadron decay or from photon conversions. Non-prompt leptons contribute a significant source of background to the 3ℓ, 2ℓSC, and 2ℓSC+τ channels and are estimated using a template fit method where a simultaneous fit of the MC simulations to data is performed in several CRs, each enriched in a different source of non-prompt leptons.

Photon conversions, where high-energy photons transform into electron-positron pairs, occur through two primary mechanisms: internal conversions and material conversions. Internal conversions stem from electron-positron pair creation in a decay that might otherwise have emitted a photon. Material conversions occur when high-energy photons interact with detector materials, generating electron-positron pairs within the detector. In the 3ℓ channel, the contribution of non-prompt leptons coming from internal conversions is very small and the shape and normalisation of this background is estimated using MC simulation. Conversely, the material conversion backgrounds in the 3ℓ channel are constrained using a control region ('Mat. conv. CR' in Table 5) where leptons with a conversion vertex with radius $r > 20$ mm from the primary vertex and an invariant mass of the two opposite-charge tracks at the conversion vertex, $m_{\text{trk,trk}} < 100$ MeV. An additional requirement that the invariant mass of the three leptons be consistent with the Z boson mass is also applied to preferentially select $Z \to \ell\ell\gamma^*(\gamma^* \to \ell'\ell')$ events where one of the leptons is out of acceptance, and further enrich the region with events containing a material conversion. This region is included in the final fit with one bin and a normalisation factor of 0.66±0.13 is obtained. For the 2ℓSC channel, an internal conversion CR ('Int. conv. CR' in Table 5) is defined by requiring that the leptons are associated with a conversion vertex with radius $r < 20$ mm from the primary vertex, and an invariant mass of the two opposite-charge tracks at the primary vertex, $m_{\text{trk,trk}} < 100$ MeV. Another

CR requiring that leptons have a conversion vertex with radius $r > 20$ mm from the primary vertex and an invariant mass of the two opposite-charge tracks at the conversion vertex, $m_{\text{trk,trk}} < 100$ MeV is used to constrain material conversions. These regions are included in the final fit with one bin and normalisation factors of 1.84±0.28 and 1.30±0.39 are obtained for the internal conversion and material conversion processes, respectively. Unlike the 3ℓ channel where material conversions stem from $V\gamma$ and Z+jets events, in the 2ℓSC channel this originates mostly from top quark backgrounds, which leads to the difference in normalisation factors between the channels. Photon conversions are a negligible background to the 2ℓSC+τ channel and their shape and normalisation is taken directly from simulations.

Additional dedicated CRs are defined to estimate backgrounds originating from the decay of heavy-flavour hadrons into muons (HF-μ) or electrons (HF-e). For the HF-e (HF-μ) CR in the 3ℓ channel, the same-charge leptons ℓ_{SC1} and ℓ_{SC2} are chosen to be electrons (muons) and the PLV isolation requirements are dropped for all three leptons. Additional selections requiring that there are at least two b-tagged jets are also applied to these CRs to further enrich the heavy-flavour backgrounds. The distribution of the ΔR between ℓ_{OC} and ℓ_{SC1} in the CRs are included in the final fit and normalisation factors of 1.50±0.50 and 1.51±0.23 are obtained from the HF-e CR and HF-μ CR, respectively. Two CRs requiring at least one electron, removing the requirements on the PLV isolation, and requiring that there are two or three jets in the event, are employed in the 2ℓSC channel to estimate the HF-e background. The first CR requires that exactly one of the jets is b-tagged, while the second requires that exactly two jets are b-tagged. An analogous region is used as a HF-μ CR, where events with at least one μ are selected with the same lepton isolation requirements as in the HF-e CR. In addition, the HF-μ CR is required to have two or three jets, at least one of them b-tagged. The distribution of the ΔR between the two leptons in the first HF-e CR, and the distributions of the scalar sum of the p_{T}s of all leptons and $E_{\text{T}}^{\text{miss}}$ in the second HF-e CR and the HF-μ CR, are included in the final fit. Normalisation factors of 1.17±0.30 and 1.63±0.20 are obtained for HF-e and HF-μ backgrounds respectively. For the 2ℓSC+τ channel, the same CR definitions as for the 2ℓSC channel are applied with respect to the preselection requirements, but loosening the jet multiplicity requirements to allow events to have at least two jets. Normalisation factors of 0.87±0.09 and 0.75±0.06 are obtained for HF-e and HF-μ backgrounds respectively.

The systematic uncertainty in this template fit method for the various non-prompt lepton background components is determined by relaxing the isolation and identification criteria applied to the leptons. The templates obtained using MC simulations are compared with the shape of distributions in data after subtracting the expected contributions from processes with prompt leptons using MC simulations. For each source of non-prompt lepton backgrounds, the difference between the simulations-based template and these residual data events obtained under the adjusted criteria are considered as uncertainties in the shape of the estimates obtained under the nominal conditions.

7.3 Charge misassignment

Backgrounds where the charge of the lepton has been incorrectly assigned primarily affect the 2ℓSC channel. Such events originate from Z+jets, $t\bar{t}$ and WW processes, where one electron undergoes a hard bremsstrahlung and asymmetric conversion ($e^{\pm} \to e^{\pm}\gamma^{*} \to e^{\pm}e^{+}e^{-}$), or the track curvature is mismeasured. The rate of electron charge mismeasurement is measured in data by taking the ratio of same-charge and opposite-charge pairs of electrons in a high purity sample of $Z \to e^{+}e^{-}$ events, following the method described in Ref. [81]. The CR is defined by selecting events satisfying the 2ℓSC preselection criteria, but removing the lepton charge requirements and requiring that there are less than two jets in the event. The charge misidentification rates are measured separately for prompt electrons, and electrons that originated in

either an internal conversion or a material conversion (following analogous selection requirements as used for the non-prompt lepton CRs described above). Rates are calculated as a function of p_{T} and η of the electrons in each category and range from 10^{-5} for low-p_{T} prompt electrons to 10^{-1} for high-p_{T} electrons with a large-radius conversion, but are more typically around 10^{-3}. The measured charge misassignment rate is applied to data events satisfying the requirements of the 2ℓSC channel preselection, but requiring that the two leptons have opposite charge. Uncertainties in the method are evaluated by comparing the nominal rates with those computed using simulated $Z \to e^+e^-$ events, and by varying the requirements on the dielectron invariant mass used to select $Z \to e^+e^-$ events. The muon charge misassignment rate is negligible in the p_{T} range considered in this analysis. Processes with a misassigned charge constitute less than 1% of events in the 3ℓ and 2ℓSC+τ signal regions and for these channels their contribution is taken from the MC simulations.

7.4 Misidentified hadronic taus

Quark- or gluon-initiated jets that are incorrectly reconstructed as a $\tau_{\text{had-vis}}$ (fake-$\tau_{\text{had-vis}}$) are an important background to the 2ℓSC+τ, 2ℓ+2τ, and ℓ+2τ channels. In the 2ℓSC+τ channel, background processes where a jet fakes the $\tau_{\text{had-vis}}$ are estimated by deriving scale factors to correct the rate of jets to be misidentified as hadronic taus in MC to match the rate in data. The scale factors are derived by comparing the rates of jets to pass the $\tau_{\text{had-vis}}$ identification requirements in data, to the rate in MC simulations, in a control region defined by applying the same preselection requirements described in Section 5 but requiring that the two light leptons have opposite-sign charge and that their invariant mass is not compatible with m_Z. Contributions from processes containing real $\tau_{\text{had-vis}}$ or prompt leptons are subtracted from data using predictions from MC simulations before computing the ratio. Scale factors are derived separately for one- and three-prong taus, as a function of the $\tau_{\text{had-vis}}$ p_{T}. The derived scale factors are applied to the relevant simulated events in the signal region and are in the range 0.68–0.86 (0.48–0.82) for one-prong (three-prong) taus. Two VRs, enriched with fake-$\tau_{\text{had-vis}}$ in Z+jets and $t\bar{t}$ events are respectively defined by modifying the CR to require that the invariant mass of the two light leptons is consistent with the Z boson mass, and by requiring that there are exactly two jets in the event, exactly one of which passes the b-tagging requirements. The largest difference in each region and p_{T} bin, between the scale factors derived in the nominal CR and those derived in the VRs, is taken as an uncertainty on the method. An additional source of systematic uncertainty is considered by varying the real-$\tau_{\text{had-vis}}$ contribution from simulations up and down by 50%. The total uncertainty on the scale factors ranges from 20% to 34%, depending on the p_{T} range and number of prongs considered.

Fake-$\tau_{\text{had-vis}}$ backgrounds in the 2ℓ+2τ and ℓ+2τ channels are estimated from data using the fake-factor method described in Ref. [102]. The fake-factors are estimated in a CR enriched in Z+jets events that is sub-divided into events with one or more real $\tau_{\text{had-vis}}$, and events with one or more fake $\tau_{\text{had-vis}}$. The fake-factors are calculated from the ratio of the numbers of events in each sub-region, and are derived as a function of p_{T}, $|\eta|$ and number of prongs of the (anti-)$\tau_{\text{had-vis}}$. The fake-factors are then applied to fake-$\tau_{\text{had-vis}}$ CRs that apply the preselection requirements of the 2ℓ+2τ and ℓ+2τ channels, but require that one or both of the two hadronic taus instead satisfy the anti-$\tau_{\text{had-vis}}$ definition. Real $\tau_{\text{had-vis}}$ passing the anti-$\tau_{\text{had-vis}}$ requirements are corrected for using MC simulations in all CRs. The fake-factors are also estimated in a VR enriched in $t\bar{t}$ events in order to check the dependency of the fake-factors to light-flavour quark, heavy-flavour quark, or gluon-initiated jets. The measured fake-factors in the $t\bar{t}$ VR are consistent within statistical uncertainties with the nominal ones, but the difference (~30%) is treated as a systematic uncertainty arising from the different jet compositions in each region. The contribution of real

$\tau_{\text{had-vis}}$ passing the anti-$\tau_{\text{had-vis}}$ requirements is varied up and down by 15% and the impact on the derived fake-factors is considered as an additional source of uncertainty. The fake-$\tau_{\text{had-vis}}$ background estimate is validated in VRs that follow the signal region definition but require that the two $\tau_{\text{had-vis}}$ have the same-sign charge. Good agreement between the data and the background prediction is observed in the 2ℓ+2τ and ℓ+2τ channel VRs, within the available statistical precision. A 10% discrepancy is observed in the ℓ+2τ VR, which is then conservatively considered as an additional uncertainty on the fake-$\tau_{\text{had-vis}}$ background estimate in both the 2ℓ+2τ and ℓ+2τ channels.

7.5 Non-resonant $\gamma\gamma$ production

Non-resonant $\gamma\gamma$ production originates from $\gamma\gamma$+jets, $V\gamma\gamma$, and $t\bar{t}\gamma\gamma$ processes, as well as from processes where a jet is incorrectly identified as a photon. This $\gamma\gamma$-continuum background is expected to have a smoothly falling shape. It is modelled using a functional form chosen by fitting the diphoton invariant mass distribution in sidebands around the Higgs boson mass [105 GeV $< m_{\gamma\gamma} <$ 120 GeV, 130 GeV $< m_{\gamma\gamma} <$ 160 GeV] in a CR in data, following the methodology described in Refs. [25, 80]. The CR is defined by requiring that events have no P-type leptons (as defined in Table 2) or $\tau_{\text{had-vis}}$, have one ($\gamma\gamma$+ℓ and $\gamma\gamma$+τ channels) or two ($\gamma\gamma$+$2(\ell,\tau)$ channel) jets, and pass all other preselection requirements defined in Section 5. A first-order exponential function is observed to provide the best fit to the background model in all regions. This function is used to generate a background histogram, with the fit parameters left as free parameters when fitting to the data in sidebands. The fit is performed separately in each region and each channel, but in the $\gamma\gamma$+ℓ and $\gamma\gamma$+τ channels the BDT Medium and BDT Tight regions are combined to obtain the fit parameters, and then the background template is normalised to the sidebands in each region separately.

The potential bias associated with the choice of functional form to model the continuum background or absorb a signal is evaluated in each signal region by fitting the background template using a model with free parameters following the prescriptions described in Refs. [80, 103]. Uncertainties of up to 4% due to this 'spurious signal' uncertainty are observed. An additional source of uncertainty in the shape of the non-resonant background caused by differences in the background composition between the signal region and the CR is estimated using MC simulations of photon pairs produced in association with one or two jets. The background template is derived using these simulated samples in the CR region, requiring exactly zero P-type leptons and $\tau_{\text{had-vis}}$, and comparing this to the background template obtained from the simulated samples when the same lepton and $\tau_{\text{had-vis}}$ requirements of the respective signal regions are applied. The difference between these two estimates is taken as the uncertainty on the nominal background estimate derived from data. Uncertainties on the background normalisation of ±13.1% (±8.4%) are measured in the Medium (Tight) BDT-score regions of the $\gamma\gamma$+ℓ channel, ±12.4% (±8.0%) in the Medium (Tight) BDT-score regions of the $\gamma\gamma$+τ channel, and less than 2% in all other regions.

8 Systematic uncertainties

For every channel, the total uncertainty is dominated by the statistical uncertainty on the number of data events in the signal region. Experimental sources of systematic uncertainty due to the detector response and background modelling are considered, as are theoretical uncertainties on the normalisation and shape of signal and background processes considered. The finite statistics of MC simulations used in the analysis are also considered as a source of systematic uncertainty. The impact of the different sources of uncertainty

on the expected μ_{HH} upper limit at 95% CL is summarised in Table 7 for the combination of all channnels, as well as for the combinations of the ML channels and $\gamma\gamma$+ML channels separately.

Table 7: Breakdown of the relative contributions to the uncertainties on the expected μ_{HH} upper limit at 95% CL , as determined in the likelihood fit to data described in Section 9, for combinations of the ML channels, the $\gamma\gamma$+ML channels, and all channels. The impact of the uncertainties is quantified as the relative variation of the expected upper limit when re-evaluating the profile likelihood ratio after fixing a nuisance parameter to its best-fit value, while all other nuisance parameters are allowed to float.

Uncertainty source	Relative impact of systematic uncertainties [%]		
	ML channels	$\gamma\gamma$+ML channels	Combination
Systematic	22	14	19
MC statistics	5	<1	3
Experimental	5	<1	3
Detector response	4	<1	3
Luminosity and pile-up	<1	<1	<1
Electrons	<1	<1	<1
Muons	<1	<1	<1
$\tau_{\text{had-vis}}$	<1	<1	<1
Jets and $E_{\text{T}}^{\text{miss}}$	3	<1	2
Flavour-tagging	1	<1	<1
Photons	<1	<1	<1
Background estimation	<1	<1	<1
Theoretical	13	14	13
Signal	10	12	11
Backgrounds	4	2	3
Top quark	1	-	<1
Vector boson	3	-	2
Single Higgs	1	2	1
Other	<1	-	<1

8.1 Experimental uncertainties

The uncertainty in the combined 2015–2018 integrated luminosity is 0.83% [41], obtained using the LUCID-2 detector [104] for the primary luminosity measurements, complemented by measurements using the inner detector and calorimeters. An uncertainty arising from the correction of the pile-up distribution in simulation to that in data is also considered.

The impact of uncertainties in the trigger, reconstruction, identification and isolation efficiencies of electrons [81, 95], muons [83, 96], and photons [81, 95] are considered. An additional uncertainty in the track-to-vertexing matching is applied to muons. Reconstruction and identification efficiency uncertainties on $\tau_{\text{had-vis}}$ [105] are also considered, along with the uncertainty associated to measurements of the tau energy scale, and the efficiency of the electron veto used in the $\tau_{\text{had-vis}}$ selection.

Jet energy scale and resolution uncertainties [106] and the uncertainty in the efficiency of matching jets to the primary vertex [107] are considered. These energy scale and resolution uncertainties, in addition to an

uncertainty in the tracks matched to the primary vertex but not associated with other reconstructed objects in the event, are propagated to the $E_{\mathrm{T}}^{\mathrm{miss}}$ calculation [94, 108]. Uncertainties in the b-jet tagging efficiency and misidentification rates are estimated using $t\bar{t}$ events [92, 109] for b- and c-jets, and Z+jets events for light-flavour jets [110], and considered in the analysis.

Systematic uncertainties associated with the experimental methods used for the background estimation are described in Section 7.

8.2 Theoretical uncertainties

Several sources of theoretical uncertainty impacting the signal models are considered. The uncertainties linked to the modelling of the parton shower and underlying event are assessed by comparing the nominal sample, where the showering is modeled using Pythia 8, with an alternative sample that uses Herwig 7. Uncertainties in the matrix element calculation are assessed by varying the factorisation and renormalisation scales employed in the generator, either independently or concurrently, by a factor of two. Theoretical uncertainties related to the ggF HH cross-section, stemming from uncertainties in the PDF and α_s ($\pm 3.0\%$), as well as the selection of renormalisation scheme and the top quark mass scheme ($^{+6\%}_{-23\%}$) [14, 15] are also considered. Uncertainties on the VBF HH cross-section are also considered and are dominated by the uncertainty in the PDF and α_s ($\pm 2.1\%$). These cross-section uncertainties are factored into the determination of the upper limits on the HH signal strength. Theoretical uncertainties associated with the branching ratios of the Higgs bosons [111] range from 1.2% to 2.1% and are also considered but are negligible.

Background modelling uncertainties due to the choice of generator for the hard scatter and parton shower are considered by comparing them with alternative simulation setups, as detailed in Table 1, where available. Uncertainties due to the choice of renormalisation and factorisation scales are evaluated by varying these by factors of 0.5 and 2, relative to the nominal scales. For background processes where the normalisation is determined from control regions in data, no uncertainty in the cross-section is considered. Uncertainties of 20% [112], and 5% [113] are considered on the normalisations of the $t\bar{t}t\bar{t}$, and tZ/γ^* processes, respectively. Conservatively, a 50% uncertainty in the normalisation of $t\bar{t}t$, tW, tZ/γ^*, $t\bar{t}W^+W^-$, and VVV backgrounds is applied. Theoretical uncertainties associated with single Higgs boson production cross-sections due to missing higher-order QCD corrections, the effects of PDF and α_s uncertainties, and the uncertainties in the branching fractions, are taken from Ref. [111]. The total theoretical uncertainties on the different single Higgs production modes are 9% for gluon-fusion, 3% for VBF, 3% for WH, 4% for ZH, and 11% for $t\bar{t}H$.

9 Statistical treatment and results

Measurements of the HH signal strength are obtained using a binned likelihood function $L(\alpha, \theta)$, following the method described in Ref. [114]. The variable α represents the parameters of interest (POI) associated with the measurement, while θ represents nuisance parameters corresponding to the systematic uncertainties described in Section 8 and background parameters that are constrained by control regions in data. The global likelihood function $L(\alpha, \theta)$ is the result of multiplying the likelihood functions in each of the nine signal regions and the 19 CRs indicated in Tables 5 and 6. For each channel, the likelihood function is derived from the respective signal and background models of the probability density functions for the

variable of interest. These models take into account the expected signal and background yields for given values of α and θ, as well as the observed distribution of the discriminating variable in each channel – the BDT output score distribution for each of the ML channels, and $m_{\gamma\gamma}$ for the $\gamma\gamma$+ML channels.

Upper limits are set on the HH signal strength, μ_{HH} (defined as the ratio of the HH production cross-section, including only the ggF and VBF processes, to its SM prediction of 32.7 fb) at 95% CL, using the profile-likelihood-ratio test statistic and the modified frequentist CL_s technique [115] in the asymptotic approximation [116]. Asimov datasets [116] are used to derive the expected limits, with all nuisance parameters set to values derived from the fit to the data, and the parameters of interest fixed to the values corresponding to the hypothesis being tested. The 95% CL limits on the signal strength for individual channels, the statistical combinations of the ML and $\gamma\gamma$+ML signal categories, and the combination of all channels, is shown in Figure 8. The overall combination yields an observed 95% CL upper limit on μ_{HH} of 18, with expected upper limits of 11 in the absence of HH production, and 12 for the SM case. If systematic uncertainties are neglected then the expected limit is 9 when assuming no HH production.

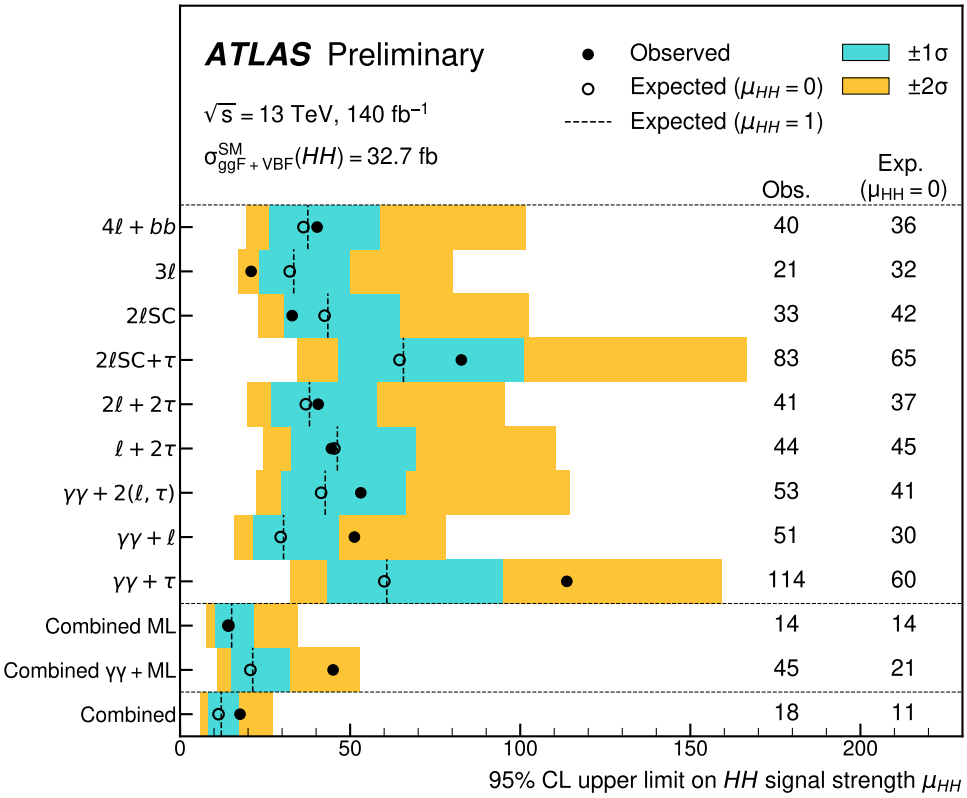

Figure 8: Observed (filled circles) and expected (open circles) 95% CL upper limits on the signal strength for HH production in the background-only ($\mu_{HH} = 0$) hypothesis. The dashed lines indicate the expected 95% CL upper limits on μ_{HH} in the SM hypothesis ($\mu_{HH} = 1$). The turquoise and yellow bands indicate the $\pm 1\sigma$ and $\pm 2\sigma$ variations on the expected limit with respect to the background-only hypothesis due to statistical and systematic uncertainties, respectively. Results are shown individually for the different search channels, the statistical combination of ML and $\gamma\gamma$+ML channels separately, and the statistical combination of all channels. The Higgs boson is assumed to have a mass of 125 GeV when deriving the predicted SM cross-section.

10 Conclusion

A search for Higgs pair-production targeting the $bbZZ$, $4V$, $VV\tau\tau$, 4τ, $\gamma\gamma VV$ and $\gamma\gamma\tau\tau$ decay channels is explored for the first time in ATLAS. Final states are categorised based on the multiplicity of light charged leptons (electrons or muons), hadronically decaying taus, and photons. BDTs are used to separate signal from backgrounds in eight of the nine explored channels. The main background processes to the ML channels involving vector bosons and top-quarks are estimated from MC simulation and normalised to data. Background processes involving charge-misidentification of leptons, non-prompt leptons, misidentification of hadronic taus, and non-resonant $\gamma\gamma$ production are estimated using data-driven methods. The analysis is performed with proton–proton collision data at $\sqrt{s}$ = 13 TeV collected from 2015 to 2018 with the ATLAS detector at the LHC, corresponding to an integrated luminosity of 140 fb^{-1}.

Observed (expected) limits of 18 (11) times the SM prediction are set on the HH signal strength. The sensitivity of the channels presented in this study are comparable to the other channels already investigated by ATLAS and CMS and will contribute to improve the global sensitivity to HH production. The sensitivity of the results in all channels is limited by the available data statistics.

Appendix

The BDT input variables used in the different ML channels are summarised in Tables 8 and 9 and in the $\gamma\gamma$+ℓ and $\gamma\gamma$+τ channels in Table 10.

Table 8: Variables used as inputs to the 4ℓ+bb, 3ℓ, and 2ℓSC channel BDTs. i and j are the indices of the p_{T}-ordered objects referred to.

Variable	Description	4ℓ+bb	3ℓ	2ℓSC
$p_{\mathrm{T}}(\ell_i)$	p_{T} of the ith lepton	$i = 1,2,3,4$	-	-
$\eta(\ell_i)$	η of the ith lepton	$i = 1,2,3,4$	-	$i = 1,2$
$E_{\mathrm{T}}^{\Delta R<0.3}/E_{\mathrm{T}}(\ell_i)$	Isolation metric ($E_{\mathrm{T}}^{\Delta R<0.3}$ = total energy deposited in a cone of radius $R = 0.3$ around the lepton, and E_{T} = lepton energy)	$i = 1,2,3,4$	-	-
Dilepton type	$\mu\mu = 1$, $e\mu/\mu e = 2$, $ee = 3$	-	-	✓
m_{ℓ_i,ℓ_j}	Invariant mass of the ith and jth leptons	$i,j = 1,2$ $i,j = 3,4$	$i,j = 1,2$ $i,j = 1,3$ $i,j = 2,3$	$i,j = 1,2$
$m_{\ell\ell}^{Z\text{-match}}$	Invariant mass of pair of SFOS leptons that minimises the difference with the Z boson mass	-	✓	-
$m_{\ell\ell}^{\text{other}}$	Invariant mass of the other SFOS lepton pair	✓	-	-
min. $m_{\ell\ell}^{\text{SFOS}}$	Minimum invariant mass out of all SFOS pairs	-	✓	-
$m_{4\ell}$	Invariant mass of four leptons	✓	-	-
$m_{3\ell}$	Invariant mass of three leptons	-	✓	-
$m_{\ell_i,\text{close-jet}}$	Invariant mass of the ith lepton and its closest jet	-	$i = 1,2,3$	$i = 1,2$
$m_{3\ell\text{jj}}$	Invariant mass of the three leptons and the leading (or two leading, for events with $N_{\text{jet}} \geq 2$) jets	-	✓	-
m_{jj}	Invariant mass of the two leading jets	✓	-	-
m_{all}	Invariant mass of all selected objects in the event	-	-	✓
$m_{\mathrm{T}}^{W}(\ell_i, E_{\mathrm{T}}^{\text{miss}})$	Transverse mass of a leptonically decaying W-boson reconstructed from the ith lepton and its closest jet	-	-	$i = 1,2$
$\Delta\eta(\ell_i,\ell_j)$	Separation in η between the ith and jth leptons	-	-	$i = 1,2$
$\Delta R(\ell_i,\ell_j)$	Separation in R between the ith and jth leptons		$i,j = 1,2$ $i,j = 1,3$ $i,j = 2,3$	$i,j = 1,2$
$\Delta R(\ell_i,\text{close-j})$	Separation in R between the ith lepton and its closest jet	-	$i = 1,2,3$	$i = 1,2$
min. $\Delta R(\ell,\text{jet})$	Minimum separation in R between any lepton and any jet	-	-	✓
L_{T}	Scalar sum of the p_{T} of all leptons and the $E_{\mathrm{T}}^{\text{miss}}$	-	✓	✓
H_{T}	Scalar sum of the p_{T} of all jets	-	✓	✓
S_{T}	Scalar sum of the p_{T} of all objects in the event	✓	✓	-
ΣQ_ℓ	Sum of all lepton charges	-	-	✓
N_{jet}	Number of jets in the event	-	-	✓
$N_{b\text{-jet}}$	Number of b-jets in the event	✓	-	-
$p_{\mathrm{T}}(\text{j}_1)$	p_{T} of the leading jet	✓	-	-
$p_{\mathrm{T}}(\text{jj})$	p_{T} of the leading di-jet system	✓	-	-
$E_{\mathrm{T}}^{\text{miss}}$	Magnitude of the missing transverse momentum	✓	✓	✓
$\Delta\phi(E_{\mathrm{T}}^{\text{miss}},\text{j}_1)$	ϕ angle between the $E_{\mathrm{T}}^{\text{miss}}$ and the leading jet	✓	-	-

Table 9: Variables used as inputs to the 2ℓSC+τ, 2ℓ+2τ, and ℓ+2τ channel BDTs. i and j are the indices of the p_{T}-ordered objects referred to.

Variable	Description	2ℓSC+τ	2ℓ+2τ	ℓ+2τ
Dilepton type	$\mu\mu$ = 1, $e\mu$/μe = 2, ee = 3	-	✓	-
m_{ℓ_i,ℓ_j}	Invariant mass of the ith and jth leptons	-	$i,j = 1,2$	-
$m_{\ell_i,\text{close-jet}}$	Invariant mass of the ith lepton and its closest jet	$i = 1$	-	$i = 1$
$m_{\ell_i \mathrm{j}_j}$	Invariant mass of the ith lepton and jth jet	$i,j = 1,1$ $i,j = 1,2$ $i,j = 2,1$	-	-
$\Delta\eta(\ell_i,\ell_j)$	Separation in η between the ith and jth leptons	$i,j = 1,2$	-	-
$\Delta R(\ell_i,\ell_j)$	Separation in R between the ith and jth leptons	$i,j = 1,2$	$i,j = 1,2$	-
$\Delta R(\ell_i,\mathrm{j}_j)$	Separation in R between the ith lepton and jth jet	$i,j = 1,1$	-	$i,j = 1,1$ $i,j = 1,2$
$\Delta R(\ell_i,\text{close-j})$	Separation in R between the ith lepton and its closest jet	$i = 1,2$	-	-
$p_{\mathrm{T}}(\mathrm{j}_1)$	p_{T} of the leading jet	-	-	✓
$E_{\mathrm{T}}^{\text{miss}}$	Magnitude of the missing transverse momentum	-	-	✓
$\theta^{\text{boost-}\ell\ell}_{\tau_{\text{had}},\text{jet}_i}$	Polar angle between the $\tau_{\text{had-vis}}$ and the ith jet after a Lorentz boost to the dilepton system	$i = 1,2$	-	-
$\Delta R^{\text{boost-}\ell_i\tau_{\text{had}}}_{\ell_i,\text{jet}_j}$	Separation in R between the ith lepton and jth jet after a Lorentz boost to the $\tau_{\text{had-vis}}$ and ith lepton system	$i,j = 1,2$ $i,j = 2,1$	-	-
$m_{\tau\tau}$	Invariant mass of the two $\tau_{\text{had-vis}}$	-	✓	✓
$\Delta R(\ell_i,\tau_j)$	Separation in R between the ith lepton and jth $\tau_{\text{had-vis}}$	-	$i,j = 2,1$	-
$\Delta R(\ell_i,\tau\tau)$	Separation in R between the ith lepton and the di-$\tau_{\text{had-vis}}$ system	-	$i = 1$	$i = 1$
$m_{\ell_i\tau_j}$	Invariant mass of the ith lepton and jth $\tau_{\text{had-vis}}$	-	$i,j = 2,1$	-
$m_{\ell\tau\tau}$	Invariant mass of the lepton and two $\tau_{\text{had-vis}}$	-	-	✓
$\vec{p_{\mathrm{T}}}(\ell) + \vec{p_{\mathrm{T}}}(\text{close-j})$	Vector sum of the p_{T}s of the lepton and its closest jet	-	-	✓
$\vec{p_{\mathrm{T}}}(\tau_1) + \vec{p_{\mathrm{T}}}(\tau_2)$	Vector sum of the p_{T}s of the two $\tau_{\text{had-vis}}$	-	✓	✓

Table 10: Variables used as inputs to the $\gamma\gamma$+ℓ and $\gamma\gamma$+τ channel BDTs. Photons and jets are p_{T} ordered.

Variable	Description	$\gamma\gamma$+ℓ	$\gamma\gamma$+τ
$p_{\mathrm{T}}(\gamma\gamma)$	p_{T} of the diphoton system	✓	✓
$p_{\mathrm{T}}(\ell)$	p_{T} of the lepton	✓	-
$p_{\mathrm{T}}(\tau_{\text{had-vis}})$	p_{T} of the $\tau_{\text{had-vis}}$	-	✓
$E_{\mathrm{T}}^{\text{miss}}$	Magnitude of the missing transverse momentum	✓	✓
$\phi(E_{\mathrm{T}}^{\text{miss}})$	ϕ direction of the $E_{\mathrm{T}}^{\text{miss}}$	-	✓
$\eta(\ell E_{\mathrm{T}}^{\text{miss}})$	η of the lepton-$E_{\mathrm{T}}^{\text{miss}}$ system	✓	-
$\eta(\gamma_i)$	η of the ith photon	-	✓
$N_{\text{central-jets}}$	Number of jets with $\lvert\eta\rvert < 2.5$	✓	✓
$\Delta R(\ell, E_{\mathrm{T}}^{\text{miss}})$	ΔR between the lepton and the $E_{\mathrm{T}}^{\text{miss}}$	✓	-
$\Delta R(\gamma\gamma, \ell E_{\mathrm{T}}^{\text{miss}})$	ΔR between the diphoton system and the lepton-$E_{\mathrm{T}}^{\text{miss}}$ system	✓	-
$\Delta\phi(\ell/\tau_{\text{had}}, \gamma\gamma)$	Separation in ϕ between the lepton or $\tau_{\text{had-vis}}$ and the diphoton system	✓	✓
$\Delta\phi(\gamma_1, \gamma\gamma)$	Separation in ϕ between the leading photon and the diphoton system	✓	✓
$\min.\Delta\phi(E_{\mathrm{T}}^{\text{miss}}, \mathrm{j}, \ell)$	Minimum ϕ angle between the $E_{\mathrm{T}}^{\text{miss}}$, the lepton, and any jet	✓	-
$\Delta\phi(E_{\mathrm{T}}^{\text{miss}}, \gamma\gamma)$	Separation in ϕ between the $E_{\mathrm{T}}^{\text{miss}}$ and the diphoton system	✓	✓

References

[1] ATLAS Collaboration, *Observation of a new particle in the search for the Standard Model Higgs boson with the ATLAS detector at the LHC*, Phys. Lett. B **716** (2012) 1, arXiv: 1207.7214 [hep-ex] (cit. on p. 2).

[2] CMS Collaboration, *Observation of a new boson at a mass of 125 GeV with the CMS experiment at the LHC*, Phys. Lett. B **716** (2012) 30, arXiv: 1207.7235 [hep-ex] (cit. on p. 2).

[3] B. Horn, *The Higgs Field and Early Universe Cosmology: A (Brief) Review*, Physics **2** (2020) 503 (cit. on p. 3).

[4] M. Reichert et al., *Probing baryogenesis through the Higgs boson self-coupling*, Phys. Rev. D **97** (7 2018) 075008, arXiv: 1711.00019 [hep-ph] (cit. on p. 3).

[5] A. Noble and M. Perelstein, *Higgs self-coupling as a probe of the electroweak phase transition*, Phys. Rev. D **78** (2008) 063518, arXiv: 0711.3018 [hep-ph] (cit. on p. 3).

[6] F. Bezrukov and M. Shaposhnikov, *The Standard Model Higgs boson as the inflaton*, Phys. Lett. B **659** (2008) 703, arXiv: 0710.3755 [hep-th] (cit. on p. 3).

[7] T. Markkanen, A. Rajantie and S. Stopyra, *Cosmological Aspects of Higgs Vacuum Metastability*, Frontiers in Astronomy and Space Sciences **5** (2019) 40, arXiv: 1809.06923 [astro-ph.CO] (cit. on p. 3).

[8] S. Dawson, S. Dittmaier and M. Spira, *Neutral Higgs-boson pair production at hadron colliders: QCD corrections*, Phys. Rev. D **58** (1998) 115012, arXiv: hep-ph/9805244 [hep-ph] (cit. on p. 3).

[9] S. Borowka et al., *Higgs Boson Pair Production in Gluon Fusion at Next-to-Leading Order with Full Top-Quark Mass Dependence*, Phys. Rev. Lett. **117** (2016) 012001, arXiv: 1604.06447 [hep-ph], Erratum: Phys. Rev. Lett. **117** (2016) 079901 (cit. on pp. 3, 6).

[10] J. Baglio et al., *Gluon fusion into Higgs pairs at NLO QCD and the top mass scheme*, Eur. Phys. J. C. **79** (2019) 459, arXiv: 1811.05692 [hep-ph] (cit. on p. 3).

[11] D. de Florian and J. Mazzitelli, *Higgs Boson Pair Production at Next-to-Next-to-Leading Order in QCD*, Phys. Rev. Lett. **111** (2013) 201801, arXiv: 1309.6594 [hep-ph] (cit. on p. 3).

[12] D. Y. Shao, C. S. Li, H. T. Li and J. Wang, *Threshold resummation effects in Higgs boson pair production at the LHC*, JHEP **07** (2013) 169, arXiv: 1301.1245 [hep-ph] (cit. on p. 3).

[13] D. de Florian and J. Mazzitelli, *Higgs pair production at next-to-next-to-leading logarithmic accuracy at the LHC*, JHEP **09** (2015) 053, arXiv: 1505.07122 [hep-ph] (cit. on p. 3).

[14] M. Grazzini et al., *Higgs boson pair production at NNLO with top quark mass effects*, JHEP **05** (2018) 059, arXiv: 1803.02463 [hep-ph] (cit. on pp. 3, 25).

[15] J. Baglio et al., $gg \to HH$ *: Combined uncertainties*, Phys. Rev. D **103** (2021) 056002, arXiv: 2008.11626 [hep-ph] (cit. on pp. 3, 25).

[16] J. Baglio et al., *The measurement of the Higgs self-coupling at the LHC: theoretical status*, JHEP **04** (2013) 151, arXiv: 1212.5581 [hep-ph] (cit. on p. 3).

[17] R. Frederix et al., *Higgs pair production at the LHC with NLO and parton-shower effects*, Phys. Lett. B **732** (2014) 142, arXiv: 1401.7340 [hep-ph] (cit. on p. 3).

[18] L.-S. Ling et al., *NNLO QCD corrections to Higgs pair production via vector boson fusion at hadron colliders*, Phys. Rev. D **89** (2014) 073001, arXiv: 1401.7754 [hep-ph] (cit. on p. 3).

[19] F. A. Dreyer and A. Karlberg, *Fully differential vector-boson fusion Higgs pair production at next-to-next-to-leading order*, Phys. Rev. D **99** (2019) 074028, arXiv: 1811.07918 [hep-ph] (cit. on p. 3).

[20] F. A. Dreyer and A. Karlberg, *Vector-boson fusion Higgs pair production at N^3LO*, Phys. Rev. D **98** (2018) 114016, arXiv: 1811.07906 [hep-ph] (cit. on p. 3).

[21] ATLAS Collaboration, *Search for Higgs boson pair production in the two bottom quarks plus two photons final state in pp collisions at $\sqrt{s}$ = 13 TeV with the ATLAS detector*, Phys. Rev. D **106** (2022) 052001, arXiv: 2112.11876 [hep-ex] (cit. on pp. 3, 4).

[22] ATLAS Collaboration, *Search for resonant and non-resonant Higgs boson pair production in the $b\bar{b}\tau^+\tau^-$ decay channel using 13 TeV pp collision data from the ATLAS detector*, JHEP **07** (2023) 040, arXiv: 2209.10910 [hep-ex] (cit. on pp. 3, 4).

[23] ATLAS Collaboration, *Search for nonresonant pair production of Higgs bosons in the $b\bar{b}b\bar{b}$ final state in pp collisions at $\sqrt{s}$ = 13 TeV with the ATLAS detector*, Phys. Rev. D **108** (2023) 052003, arXiv: 2301.03212 [hep-ex] (cit. on p. 3).

[24] ATLAS Collaboration, *Constraints on the Higgs boson self-coupling from single- and double-Higgs production with the ATLAS detector using pp collisions at $\sqrt{s}$ = 13 TeV*, Phys. Lett. B **843** (2023) 137745, arXiv: 2211.01216 [hep-ex] (cit. on p. 4).

[25] ATLAS Collaboration, *Studies of new Higgs boson interactions through nonresonant HH production in the $b\bar{b}\gamma\gamma$ final state in pp collisions at $\sqrt{s}$ = 13 TeV with the ATLAS detector*, (2023), arXiv: 2310.12301 [hep-ex] (cit. on pp. 4, 23).

[26] ATLAS Collaboration, *Search for the non-resonant production of Higgs boson pairs via gluon fusion and vector-boson fusion in the $b\bar{b}\tau^+\tau^-$ final state in proton–proton collisions at $\sqrt{s}$ = 13 TeV with the ATLAS detector*, ATLAS-CONF-2023-071, 2023, URL: https://cds.cern.ch/record/2882132 (cit. on p. 4).

[27] ATLAS Collaboration, *Search for non-resonant Higgs boson pair production in the $2b + 2\ell + E_T^{miss}$ final state in pp collisions at $\sqrt{s}$ = 13TeV with the ATLAS detector*, (2023), arXiv: 2310.11286 [hep-ex] (cit. on p. 4).

[28] CMS Collaboration, *A portrait of the Higgs boson by the CMS experiment ten years after the discovery*, Nature **607** (2022) 60, arXiv: 2207.00043 [hep-ex] (cit. on p. 4).

[29] CMS Collaboration, *Search for nonresonant Higgs boson pair production in final states with two bottom quarks and two photons in proton–proton collisions at $\sqrt{s}$ = 13 TeV*, JHEP **03** (2021) 257, arXiv: 2011.12373 [hep-ex] (cit. on p. 4).

[30] CMS Collaboration, *Search for nonresonant Higgs boson pair production in final state with two bottom quarks and two tau leptons in proton–proton collisions at $\sqrt{s}$ = 13 TeV*, Phys. Lett. B **842** (2023) 137531, arXiv: 2206.09401 [hep-ex] (cit. on p. 4).

[31] CMS Collaboration, *Search for Higgs Boson Pair Production in the Four b Quark Final State in Proton–Proton Collisions at* $\sqrt{s}$ = 13 *TeV*, Phys. Rev. Lett. **129** (2022) 081802, arXiv: 2202.09617 [hep-ex] (cit. on p. 4).

[32] CMS Collaboration, *Search for nonresonant pair production of highly energetic Higgs bosons decaying to bottom quarks*, (2023), arXiv: 2205.06667 [hep-ex] (cit. on p. 4).

[33] CMS Collaboration, *Search for nonresonant Higgs boson pair production in the four leptons plus two b jets final state in proton–proton collisions at* $\sqrt{s}$ = 13 *TeV*, JHEP **06** (2023) 130, arXiv: 2206.10657 [hep-ex] (cit. on p. 4).

[34] CMS Collaboration, *Search for Higgs boson pairs decaying to* WW^*WW^*, $WW^*\tau\tau$, *and* $\tau\tau\tau\tau$ *in proton–proton collisions at* $\sqrt{s}$ = 13 *TeV*, JHEP **07** (2023) 095, arXiv: 2206.10268 [hep-ex] (cit. on p. 4).

[35] ATLAS Collaboration, *The ATLAS Experiment at the CERN Large Hadron Collider*, JINST **3** (2008) S08003 (cit. on p. 4).

[36] ATLAS Collaboration, *ATLAS Insertable B-Layer: Technical Design Report*, ATLAS-TDR-19; CERN-LHCC-2010-013, 2010, URL: https://cds.cern.ch/record/1291633 (cit. on p. 4), Addendum: ATLAS-TDR-19-ADD-1; CERN-LHCC-2012-009, 2012, URL: https://cds.cern.ch/record/1451888.

[37] B. Abbott et al., *Production and integration of the ATLAS Insertable B-Layer*, JINST **13** (2018) T05008, arXiv: 1803.00844 [physics.ins-det] (cit. on p. 4).

[38] ATLAS Collaboration, *Performance of the ATLAS trigger system in 2015*, Eur. Phys. J. C **77** (2017) 317, arXiv: 1611.09661 [hep-ex] (cit. on p. 5).

[39] ATLAS Collaboration, *The ATLAS Collaboration Software and Firmware*, ATL-SOFT-PUB-2021-001, 2021, URL: https://cds.cern.ch/record/2767187 (cit. on p. 6).

[40] ATLAS Collaboration, *ATLAS data quality operations and performance for 2015–2018 data-taking*, JINST **15** (2020) P04003, arXiv: 1911.04632 [physics.ins-det] (cit. on p. 6).

[41] ATLAS Collaboration, *Luminosity determination in pp collisions at* $\sqrt{s}$ = 13 *TeV using the ATLAS detector at the LHC*, Eur. Phys. J. C **83** (2023) 982, arXiv: 2212.09379 [hep-ex] (cit. on pp. 6, 24).

[42] ATLAS Collaboration, *The ATLAS Simulation Infrastructure*, Eur. Phys. J. C **70** (2010) 823, arXiv: 1005.4568 [physics.ins-det] (cit. on p. 6).

[43] S. Agostinelli et al., *GEANT4 – a simulation toolkit*, Nucl. Instrum. Meth. A **506** (2003) 250 (cit. on p. 6).

[44] T. Sjöstrand, S. Mrenna and P. Skands, *A brief introduction to PYTHIA 8.1*, Comput. Phys. Commun. **178** (2008) 852, arXiv: 0710.3820 [hep-ph] (cit. on p. 6).

[45] NNPDF Collaboration, R. D. Ball et al., *Parton distributions with LHC data*, Nucl. Phys. B **867** (2013) 244, arXiv: 1207.1303 [hep-ph] (cit. on p. 6).

[46] ATLAS Collaboration, *The Pythia 8 A3 tune description of ATLAS minimum bias and inelastic measurements incorporating the Donnachie–Landshoff diffractive model*, ATL-PHYS-PUB-2016-017, 2016, URL: https://cds.cern.ch/record/2206965 (cit. on p. 6).

[47] ATLAS Collaboration, *Measurement of the Inelastic Proton–Proton Cross Section at $\sqrt{s}$ = 13 TeV with the ATLAS Detector at the LHC*, Phys. Rev. Lett. **117** (2016) 182002, arXiv: 1606.02625 [hep-ex] (cit. on p. 6).

[48] S. Alioli, P. Nason, C. Oleari and E. Re, *A general framework for implementing NLO calculations in shower Monte Carlo programs: the POWHEG BOX*, JHEP **06** (2010) 043, arXiv: 1002.2581 [hep-ph] (cit. on pp. 6, 8).

[49] P. Nason and C. Oleari, *NLO Higgs boson production via vector-boson fusion matched with shower in POWHEG*, JHEP **02** (2010) 037, arXiv: 0911.5299 [hep-ph] (cit. on p. 6).

[50] J. Butterworth et al., *PDF4LHC recommendations for LHC Run II*, J. Phys. G **43** (2016) 023001, arXiv: 1510.03865 [hep-ph] (cit. on p. 6).

[51] T. Sjöstrand et al., *An introduction to PYTHIA 8.2*, Comput. Phys. Commun. **191** (2015) 159, arXiv: 1410.3012 [hep-ph] (cit. on p. 6).

[52] ATLAS Collaboration, *ATLAS Pythia 8 tunes to 7 TeV data*, ATL-PHYS-PUB-2014-021, 2014, URL: https://cds.cern.ch/record/1966419 (cit. on p. 6).

[53] M. Bähr et al., *Herwig++ physics and manual*, Eur. Phys. J. C **58** (2008) 639, arXiv: 0803.0883 [hep-ph] (cit. on p. 6).

[54] S. Gieseke, C. Röhr and A. Siodmok, *Colour reconnections in Herwig++*, Eur. Phys. J. C **72** (2012) 2225, arXiv: 1206.0041 [hep-ph] (cit. on p. 6).

[55] L. A. Harland-Lang, A. D. Martin, P. Motylinski and R. S. Thorne, *Parton distributions in the LHC era: MMHT 2014 PDFs*, Eur. Phys. J. C **75** (2015) 204, arXiv: 1412.3989 [hep-ph] (cit. on p. 6).

[56] J. Alwall et al., *The automated computation of tree-level and next-to-leading order differential cross sections, and their matching to parton shower simulations*, JHEP **07** (2014) 079, arXiv: 1405.0301 [hep-ph] (cit. on pp. 6, 8).

[57] NNPDF Collaboration, R. D. Ball et al., *Parton distributions for the LHC run II*, JHEP **04** (2015) 040, arXiv: 1410.8849 [hep-ph] (cit. on pp. 6, 7).

[58] P. Golonka and Z. Was, *PHOTOS Monte Carlo: a precision tool for QED corrections in Z and W decays*, Eur. Phys. J. C **45** (2006) 97, arXiv: hep-ph/0506026 (cit. on p. 7).

[59] E. Bothmann et al., *Event generation with Sherpa 2.2*, SciPost Phys. **7** (2019) 034, arXiv: 1905.09127 [hep-ph] (cit. on p. 7).

[60] T. Gleisberg and S. Höche, *Comix, a new matrix element generator*, JHEP **12** (2008) 039, arXiv: 0808.3674 [hep-ph] (cit. on p. 7).

[61] F. Buccioni et al., *OpenLoops 2*, Eur. Phys. J. C **79** (2019) 866, arXiv: 1907.13071 [hep-ph] (cit. on p. 7).

[62] F. Cascioli, P. Maierhöfer and S. Pozzorini, *Scattering Amplitudes with Open Loops*, Phys. Rev. Lett. **108** (2012) 111601, arXiv: 1111.5206 [hep-ph] (cit. on p. 7).

[63] A. Denner, S. Dittmaier and L. Hofer, *Collier: A fortran-based complex one-loop library in extended regularizations*, Comput. Phys. Commun. **212** (2017) 220, arXiv: 1604.06792 [hep-ph] (cit. on p. 7).

[64] S. Schumann and F. Krauss,
A parton shower algorithm based on Catani–Seymour dipole factorisation, JHEP **03** (2008) 038, arXiv: 0709.1027 [hep-ph] (cit. on p. 7).

[65] S. Höche, F. Krauss, M. Schönherr and F. Siegert,
A critical appraisal of NLO+PS matching methods, JHEP **09** (2012) 049, arXiv: 1111.1220 [hep-ph] (cit. on p. 7).

[66] S. Höche, F. Krauss, M. Schönherr and F. Siegert,
QCD matrix elements + parton showers. The NLO case, JHEP **04** (2013) 027, arXiv: 1207.5030 [hep-ph] (cit. on p. 7).

[67] S. Catani, F. Krauss, B. R. Webber and R. Kuhn, *QCD Matrix Elements + Parton Showers*, JHEP **11** (2001) 063, arXiv: hep-ph/0109231 (cit. on p. 7).

[68] S. Höche, F. Krauss, S. Schumann and F. Siegert, *QCD matrix elements and truncated showers*, JHEP **05** (2009) 053, arXiv: 0903.1219 [hep-ph] (cit. on p. 7).

[69] F. Siegert, *A practical guide to event generation for prompt photon production with Sherpa*, J. Phys. G **44** (2017) 044007, arXiv: 1611.07226 [hep-ph] (cit. on p. 7).

[70] S. Frixione, *Isolated photons in perturbative QCD*, Phys. Lett. B **429** (1998) 369, arXiv: hep-ph/9801442 (cit. on p. 7).

[71] D. J. Lange, *The EvtGen particle decay simulation package*, Nucl. Instrum. Meth. A **462** (2001) 152 (cit. on p. 8).

[72] S. Frixione, G. Ridolfi and P. Nason,
A positive-weight next-to-leading-order Monte Carlo for heavy flavour hadroproduction, JHEP **09** (2007) 126, arXiv: 0707.3088 [hep-ph] (cit. on p. 8).

[73] P. Nason, *A new method for combining NLO QCD with shower Monte Carlo algorithms*, JHEP **11** (2004) 040, arXiv: hep-ph/0409146 (cit. on p. 8).

[74] S. Frixione, P. Nason and C. Oleari,
Matching NLO QCD computations with parton shower simulations: the POWHEG method, JHEP **11** (2007) 070, arXiv: 0709.2092 [hep-ph] (cit. on p. 8).

[75] E. Re,
Single-top Wt-channel production matched with parton showers using the POWHEG method, Eur. Phys. J. C **71** (2011) 1547, arXiv: 1009.2450 [hep-ph] (cit. on p. 8).

[76] S. Alioli, P. Nason, C. Oleari and E. Re,
NLO single-top production matched with shower in POWHEG: s- and t-channel contributions, JHEP **09** (2009) 111, arXiv: 0907.4076 [hep-ph] (cit. on p. 8), Erratum: JHEP **02** (2010) 011.

[77] J. Pumplin et al.,
New Generation of Parton Distributions with Uncertainties from Global QCD Analysis, JHEP **07** (2002) 012, arXiv: hep-ph/0201195 (cit. on p. 8).

[78] S. Alioli, P. Nason, C. Oleari and E. Re,
NLO vector-boson production matched with shower in POWHEG, JHEP **07** (2008) 060, arXiv: 0805.4802 [hep-ph] (cit. on p. 8).

[79] ATLAS Collaboration, *Vertex Reconstruction Performance of the ATLAS Detector at* $\sqrt{s} = 13$ *TeV*, ATL-PHYS-PUB-2015-026, 2015, URL: https://cds.cern.ch/record/2037717 (cit. on p. 7).

[80] ATLAS Collaboration, *Measurement of Higgs boson production in the diphoton decay channel in pp collisions at center-of-mass energies of 7 and 8 TeV with the ATLAS detector*, Phys. Rev. D **90** (2014) 112015, arXiv: 1408.7084 [hep-ex] (cit. on pp. 7, 23).

[81] ATLAS Collaboration, *Electron and photon performance measurements with the ATLAS detector using the 2015–2017 LHC proton–proton collision data*, JINST **14** (2019) P12006, arXiv: 1908.00005 [hep-ex] (cit. on pp. 9, 10, 21, 24).

[82] ATLAS Collaboration, *Evidence for the associated production of the Higgs boson and a top quark pair with the ATLAS detector*, Phys. Rev. D **97** (2018) 072003, arXiv: 1712.08891 [hep-ex] (cit. on p. 9).

[83] ATLAS Collaboration, *Muon reconstruction and identification efficiency in ATLAS using the full Run 2 pp collision data set at* $\sqrt{s}$ = 13 *TeV*, Eur. Phys. J. C **81** (2021) 578, arXiv: 2012.00578 [hep-ex] (cit. on pp. 9, 24).

[84] ATLAS Collaboration, *Jet reconstruction and performance using particle flow with the ATLAS Detector*, Eur. Phys. J. C **77** (2017) 466, arXiv: 1703.10485 [hep-ex] (cit. on pp. 9, 10).

[85] ATLAS Collaboration, *Identification and energy calibration of hadronically decaying tau leptons with the ATLAS experiment in pp collisions at* $\sqrt{s}$ = 8 *TeV*, Eur. Phys. J. C **75** (2015) 303, arXiv: 1412.7086 [hep-ex] (cit. on p. 9).

[86] M. Cacciari, G. P. Salam and G. Soyez, *FastJet user manual*, Eur. Phys. J. C **72** (2012) 1896, arXiv: 1111.6097 [hep-ph] (cit. on pp. 9, 10).

[87] M. Cacciari, G. P. Salam and G. Soyez, *The anti-k_t jet clustering algorithm*, JHEP **04** (2008) 063, arXiv: 0802.1189 [hep-ph] (cit. on pp. 9, 10).

[88] ATLAS Collaboration, *Local Hadronic Calibration*, ATL-PHYS-PUB-2009-001-2, 2009, URL: https://cds.cern.ch/record/1112035 (cit. on p. 9).

[89] ATLAS Collaboration, *Identification of hadronic tau lepton decays using neural networks in the ATLAS experiment*, ATL-PHYS-PUB-2019-033, 2019, URL: https://cds.cern.ch/record/2688062 (cit. on pp. 9, 10).

[90] ATLAS Collaboration, *Tagging and suppression of pileup jets with the ATLAS detector*, ATLAS-CONF-2014-018, 2014, URL: https://cds.cern.ch/record/1700870 (cit. on p. 10).

[91] ATLAS Collaboration, *ATLAS flavour-tagging algorithms for the LHC Run 2 pp collision dataset*, Eur. Phys. J. C **83** (2023) 681, arXiv: 2211.16345 [physics.data-an] (cit. on p. 10).

[92] ATLAS Collaboration, *ATLAS b-jet identification performance and efficiency measurement with $t\bar{t}$ events in pp collisions at* $\sqrt{s}$ = 13 *TeV*, Eur. Phys. J. C **79** (2019) 970, arXiv: 1907.05120 [hep-ex] (cit. on pp. 10, 25).

[93] ATLAS Collaboration, *Evidence for the $H \to b\bar{b}$ decay with the ATLAS detector*, JHEP **12** (2017) 024, arXiv: 1708.03299 [hep-ex] (cit. on p. 11).

[94] ATLAS Collaboration, *Performance of missing transverse momentum reconstruction with the ATLAS detector using proton–proton collisions at* $\sqrt{s}$ = 13 *TeV*, Eur. Phys. J. C **78** (2018) 903, arXiv: 1802.08168 [hep-ex] (cit. on pp. 11, 25).

[95] ATLAS Collaboration, *Performance of electron and photon triggers in ATLAS during LHC Run 2*, Eur. Phys. J. C **80** (2020) 47, arXiv: 1909.00761 [hep-ex] (cit. on pp. 11, 24).

[96] ATLAS Collaboration, *Performance of the ATLAS muon triggers in Run 2*, JINST **15** (2020) P09015, arXiv: 2004.13447 [physics.ins-det] (cit. on pp. 11, 24).

[97] J. Friedman, *Greedy Function Approximation: A Gradient Boosting Machine*, The Annals of Statistics **29** (2000) (cit. on p. 14).

[98] ATLAS Collaboration, *Multi-Boson Simulation for* 13 *TeV ATLAS Analyses*, ATL-PHYS-PUB-2017-005, 2017, URL: https://cds.cern.ch/record/2261933 (cit. on p. 18).

[99] ATLAS Collaboration, *Observation of Electroweak Production of a Same-Sign W Boson Pair in Association with Two Jets in pp Collisions at* $\sqrt{s}$ = 13 *TeV with the ATLAS Detector*, Phys. Rev. Lett. **123** (2019) 161801, arXiv: 1906.03203 [hep-ex] (cit. on p. 18).

[100] ATLAS Collaboration, *Measurements of inclusive and differential fiducial cross-sections of* $t\bar{t}$ *production with additional heavy-flavour jets in proton–proton collisions at* $\sqrt{s}$ = 13 *TeV with the ATLAS detector*, JHEP **04** (2019) 046, arXiv: 1811.12113 [hep-ex] (cit. on p. 20).

[101] ATLAS Collaboration, *Measurement of the cross-section for W boson production in association with b-jets in pp collisions at* $\sqrt{s}$ = 7 *TeV with the ATLAS detector*, JHEP **06** (2013) 084, arXiv: 1302.2929 [hep-ex] (cit. on p. 20).

[102] ATLAS Collaboration, *Search for a new heavy scalar particle decaying into a Higgs boson and a new scalar singlet in final states with one or two light leptons and a pair of* τ*-leptons with the ATLAS detector*, JHEP **10** (2023) 009, arXiv: 2307.11120 [hep-ex] (cit. on p. 22).

[103] ATLAS Collaboration, *Recommendations for the Modeling of Smooth Backgrounds*, ATL-PHYS-PUB-2020-028, 2020, URL: https://cds.cern.ch/record/2743717 (cit. on p. 23).

[104] G. Avoni et al., *The new LUCID-2 detector for luminosity measurement and monitoring in ATLAS*, JINST **13** (2018) P07017 (cit. on p. 24).

[105] ATLAS Collaboration, *Measurement of the tau lepton reconstruction and identification performance in the ATLAS experiment using pp collisions at* $\sqrt{s}$ = 13 *TeV*, ATLAS-CONF-2017-029, 2017, URL: https://cds.cern.ch/record/2261772 (cit. on p. 24).

[106] ATLAS Collaboration, *Jet energy scale and resolution measured in proton–proton collisions at* $\sqrt{s}$ = 13 *TeV with the ATLAS detector*, Eur. Phys. J. C **81** (2021) 689, arXiv: 2007.02645 [hep-ex] (cit. on p. 24).

[107] ATLAS Collaboration, *Performance of pile-up mitigation techniques for jets in pp collisions at* $\sqrt{s}$ = 8 *TeV using the ATLAS detector*, Eur. Phys. J. C **76** (2016) 581, arXiv: 1510.03823 [hep-ex] (cit. on p. 24).

[108] ATLAS Collaboration, E_T^{miss} *performance in the ATLAS detector using 2015–2016 LHC pp collisions*, ATLAS-CONF-2018-023, 2018, URL: https://cds.cern.ch/record/2625233 (cit. on p. 25).

[109] ATLAS Collaboration, *Measurement of the c-jet mistagging efficiency in* $t\bar{t}$ *events using pp collision data at* $\sqrt{s}$ = 13 *TeV collected with the ATLAS detector*, Eur. Phys. J. C **82** (2022) 95, arXiv: 2109.10627 [hep-ex] (cit. on p. 25).

[110] ATLAS Collaboration,
Calibration of the light-flavour jet mistagging efficiency of the b-tagging algorithms with Z+jets events using $139\,fb^{-1}$ *of ATLAS proton–proton collision data at* $\sqrt{s} = 13\,TeV$,
Eur. Phys. J. C **83** (2023) 728, arXiv: 2301.06319 [hep-ex] (cit. on p. 25).

[111] D. de Florian et al.,
Handbook of LHC Higgs Cross Sections: 4. Deciphering the Nature of the Higgs Sector, (2016),
arXiv: 1610.07922 [hep-ph] (cit. on p. 25).

[112] R. Frederix, D. Pagani and M. Zaro, *Large NLO corrections in* $t\bar{t}W^{\pm}$ *and* $t\bar{t}t\bar{t}$ *hadroproduction from supposedly subleading EW contributions*, JHEP **02** (2018) 031,
arXiv: 1711.02116 [hep-ph] (cit. on p. 25).

[113] ATLAS Collaboration, *Observation of the associated production of a top quark and a Z boson in pp collisions at* $\sqrt{s} = 13\,TeV$ *with the ATLAS detector*, JHEP **07** (2020) 124,
arXiv: 2002.07546 [hep-ex] (cit. on p. 25).

[114] ATLAS Collaboration, *Combined search for the Standard Model Higgs boson in pp collisions at* $\sqrt{s} = 7\,TeV$ *with the ATLAS detector*, Phys. Rev. D **86** (2012) 032003,
arXiv: 1207.0319 [hep-ex] (cit. on p. 25).

[115] A. L. Read, *Presentation of search results: the* CL_S *technique*, J. Phys. G **28** (2002) 2693
(cit. on p. 26).

[116] G. Cowan, K. Cranmer, E. Gross and O. Vitells,
Asymptotic formulae for likelihood-based tests of new physics, Eur. Phys. J. C **71** (2011) 1554,
arXiv: 1007.1727 [physics.data-an] (cit. on p. 26), Erratum: Eur. Phys. J. C **73** (2013) 2501.